CANCER

Targeting the Siglec–sialic acid axis promotes antitumor immune responses in preclinical models of glioblastoma

Philip Schmassmann[1]*, Julien Roux[2,3], Alicia Buck[4], Nazanin Tatari[1], Sabrina Hogan[1], Jinyu Wang[5], Natalia Rodrigues Mantuano[5], Ronja Wieboldt[5], Sohyon Lee[6], Berend Snijder[6], Deniz Kaymak[1], Tomás A. Martins[1], Marie-Françoise Ritz[1], Tala Shekarian[1], Marta McDaid[1], Michael Weller[4], Tobias Weiss[4], Heinz Läubli[5,7]†, Gregor Hutter[1,8]†*

Glioblastoma (GBM) is the most aggressive form of primary brain tumor, for which effective therapies are urgently needed. Cancer cells are capable of evading clearance by phagocytes such as microglia- and monocyte-derived cells through engaging tolerogenic programs. Here, we found that high expression of sialic acid–binding immunoglobulin-like lectin 9 (Siglec-9) correlates with reduced survival in patients with GBM. Using microglia- and monocyte-derived cell-specific knockouts of Siglec-E, the murine functional homolog of Siglec-9, together with single-cell RNA sequencing, we demonstrated that Siglec-E inhibits phagocytosis by these cells, thereby promoting immune evasion. Loss of Siglec-E on monocyte-derived cells further enhanced antigen cross-presentation and production of pro-inflammatory cytokines, which resulted in more efficient T cell priming. This bridging of innate and adaptive responses delayed tumor growth and resulted in prolonged survival in murine models of GBM. Furthermore, we showed the combinatorial activity of Siglec-E blockade and other immunotherapies demonstrating the potential for targeting Siglec-9 as a treatment for patients with GBM.

INTRODUCTION

Glioblastoma (GBM) is a fatal disease without effective long-term treatment options. The current standard of care consists of tumor resection followed by adjuvant chemoradiotherapy, resulting in a median overall survival of only 14 months (*1*). Cancer immunotherapy using immune checkpoint inhibitors (ICI) has improved the outcomes of patients with different types of cancer (*2*), but clinical trials of systemic T cell ICI showed only disappointing results in GBM (*3*–*5*). This was attributed, in part, to the highly immunosuppressive immune tumor microenvironment (iTME) of GBM, which mainly consists of yolk sac–derived microglia (MG)– and monocyte-derived cells (MdCs) (*6*, *7*), together termed glioma-associated MG/macrophages (GAMs). Recent work identified GBM-associated MG and MdCs as effector cells of tumor cell phagocytosis in response to blockade of the "don't eat me" signal, CD47 (*8*–*10*). However, variability in the magnitude and durability of this response suggests the presence of additional, yet unknown, such signals.

Up-regulation of sialic acid–containing glycans on the tumor cell surface and in the tumor microenvironment (hypersialylation) is a key change in malignant tissue and is capable of affecting tumorigenesis by promoting cell invasion and metastatic potential (*11*–*14*). By engaging immunomodulatory sialic acid–binding immunoglobulin (Ig)–like lectins (Siglecs), tumor hypersialylation can trigger tolerogenic programs in different immune cell types and contributes to the establishment of the immunosuppressive iTME (*15*). Recent work has shown that inhibitory CD33-related Siglecs, including human Siglec-7, Siglec-9, and Siglec-10, promote tumor progression in various models of pancreatic, breast, and ovarian cancer by inducing a regulatory M2-like phenotype in tumor-associated macrophages (TAMs) (*15*–*18*). Similarly, increased density of sialylated glycans on cancer cells inhibits human natural killer (NK) cell activation and cytotoxicity (*19*) and facilitates induction of regulatory T cells (T_{regs}) through the engagement of Siglec-7/-9 (*20*, *21*). However, little is known about the induction of tolerogenic programs through Siglec receptors on MG and MdCs in the GBM iTME.

Here, we aimed to define the role of inhibitory Siglecs in innate-centered GBM immunotherapy. We found high *SIGLEC9* expression to be associated with worse clinical outcomes in patients with glioma and identified Siglec-E, the murine functional homolog of Siglec-9 (*18*), as an antiphagocytic signal in a preclinical GBM model. Furthermore, we showed the synergistic activity of Siglec-E blockade in combinatorial immunotherapies and demonstrated its translational potential against GBM.

RESULTS

Expression of inhibitory Siglec receptors is associated with reduced survival in patients with glioma

Stratification of patients with GBM by *SIGLEC9* expression [using the RNA sequencing (RNA-seq) dataset of the Cancer Genome

[1]Brain Tumor Immunotherapy Lab, Department of Biomedicine, University Hospital and University of Basel, 4031 Basel, Switzerland. [2]Bioinformatics Core Facility, Department of Biomedicine, University Hospital and University of Basel, 4031 Basel, Switzerland. [3]Swiss Institute of Bioinformatics, 4031 Basel, Switzerland. [4]Department of Neurology, Clinical Neuroscience Center, University Hospital and University of Zurich, 8091 Zurich, Switzerland. [5]Cancer Immunotherapy Lab, Department of Biomedicine, University Hospital and University of Basel, 4031 Basel, Switzerland. [6]Institute of Molecular Systems Biology, ETH Zurich, 8049 Zurich, Switzerland. [7]Division of Oncology, Department of Theragnostics, University Hospital of Basel, 4031 Basel, Switzerland. [8]Department of Neurosurgery, University Hospital of Basel, 4031 Basel, Switzerland.
*Corresponding author. Email: p.schmassmann@unibas.ch (P.S.); gregor.hutter@usb.ch (G.H.)
†These authors contributed equally to this work.

Atlas, TCGA (*22*)] revealed a significant ($P = 0.0221$) overall survival advantage for patients with lower *SIGLEC9* expression (Fig. 1A). Focusing on all human Siglec receptors in patients with GBM revealed a correlation between high expression and reduced overall survival only for *SIGLEC9* (fig. S1A). In contrast, in a combined low-grade glioma (LGG) patient dataset, the expression of 8 of 15 Siglec receptors correlated with reduced patient survival (fig. S1B). Among LGG, IDH^{wt} LGG showed the highest rate of worse survival-associated Siglec receptors (5 of 15, including *SIGLEC9*) (fig. S1C) (*22*). IDH^{wt} LGG is molecularly and clinically similar to GBM (*23*).

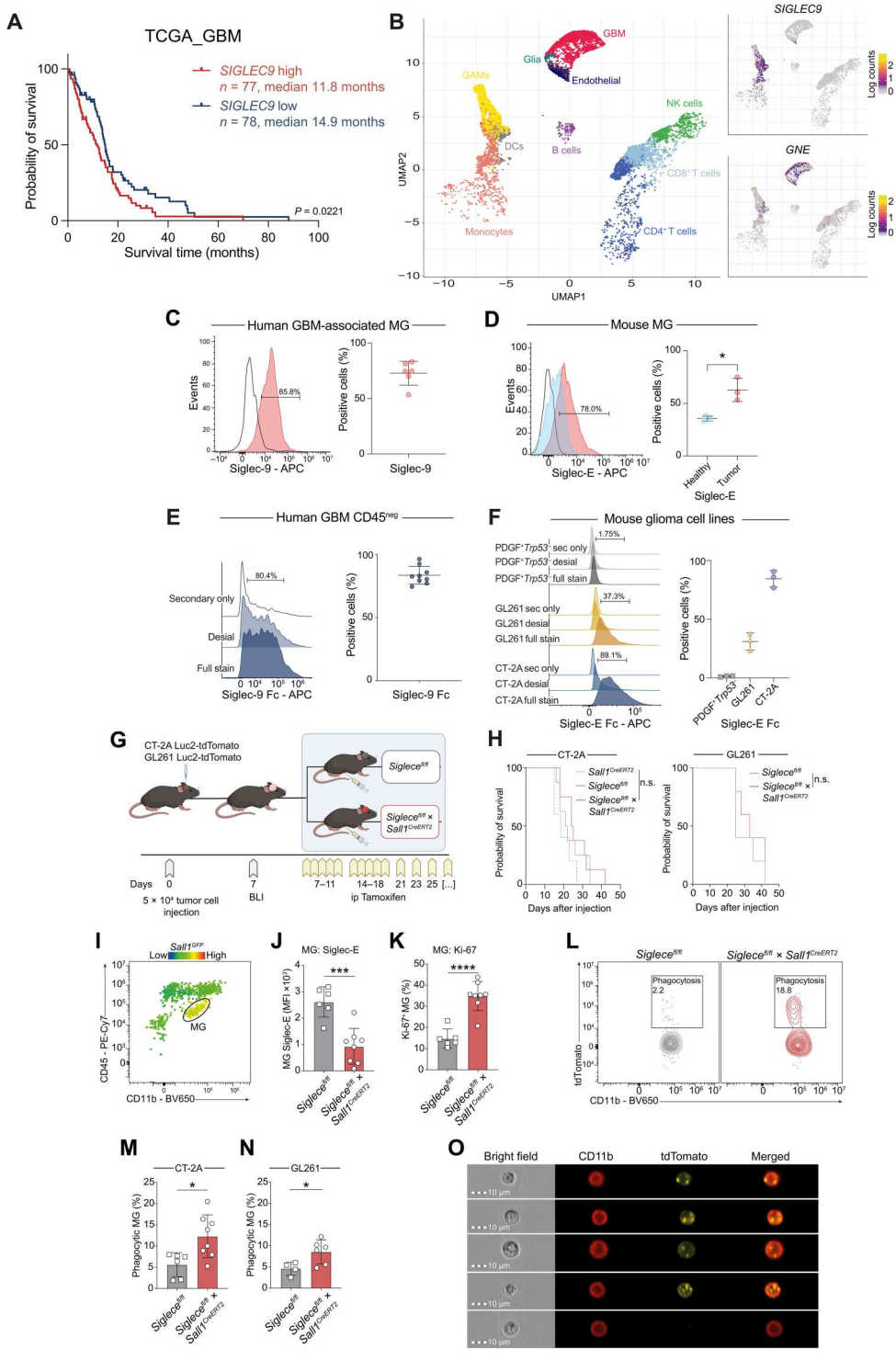

Fig. 1. High *SIGLEC9* expression is associated with reduced survival in patients with glioma, and its mouse homolog Siglec-E inhibits MG tumor cell phagocytosis. (**A**) Kaplan-Meier survival curve of patients with GBM stratified based on their *SIGLEC9* expression using the RNA-seq dataset from TCGA (*22*). The median mRNA expression value was selected as cutoff for high and low expression groups. (**B**) Uniform Manifold Approximation and Projection (UMAP) plot showing scRNA-seq cell type annotation in five primary human glioblastoma samples (*24*) (left) and UMAP showing expression of *SIGLEC9* and *GNE* in the respective clusters (right). Expression is shown as normalized $\log_2$ counts. (**C** and **D**) Representative histograms and quantification of flow cytometry analysis of Siglec-9 expression by human GBM-associated MG ($n = 6$ donors) (C) and Siglec-E expression by mouse MG from healthy and tumor-bearing mice ($n = 3$ mice per group) (D). Black histograms indicate fluorescence minus one (FMO) control. (**E** and **F**) Representative histograms and quantification of flow cytometry analysis of Siglec-9 ligand expression by human GBM $CD45^{neg}$ cells ($n = 9$ donors) (E) and Siglec-E ligand expression by mouse glioma cell lines derived from $PDGF^{+}$ $Trp53^{-}$ murine gliomas (gray) or cultured GL261 (yellow) or CT-2A (blue) cell lines ($n = 3$ independent experimental replicates) (F). Sec, secondary only; desial, enzymatic desialylation. (**G**) Schematic of experimental design. (**H**) Survival of $Sall1^{CreERT2}$, $Siglece^{fl/fl}$, and $Siglece^{fl/fl} \times Sall1^{CreERT2}$ CT-2A tumor–bearing animals (left) and $Siglece^{fl/fl}$ and $Siglece^{fl/fl} \times Sall1^{CreERT2}$ GL261 tumor–bearing animals (right) ($n = 5$ to 8 mice per group). (**I**) Gating strategy to identify $CD11b^{+}CD45^{low}$ glioma-associated MG in mouse brain tumor single-cell suspensions. The gating strategy was confirmed in $Sall1^{GFP}$ reporter mice. PE-Cy7, phycoerythrin cyanine 7; BV, brilliant violet. (**J** and **K**) Flow cytometry analysis of Siglec-E (J) and Ki-67 (K) expression in MG. (**L** to **N**) Representative contour plots showing MG CT-2A tumor cell phagocytosis (L) and quantification of MG CT-2A (M) and GL261 (N) tumor cell phagocytosis measured as the percentage of $tdTomato^{+}$ MG by flow cytometry ($n = 4$ to 8 mice per group). Results shown are from one experiment, representative of two independent experiments. (**O**) Imaging cytometry showing mouse glioma-associated MG engulfing tdTomato-expressing CT-2A tumor cells. The experiment was performed once. Data are presented as means ± SD and were analyzed by log-rank Mantel-Cox test (A and H), unpaired two-tailed Student's *t* test (D, J, K, and N), and two-tailed Mann-Whitney test (M). $*P \leq 0.05$, $***P \leq 0.001$, and $****P \leq 0.0001$; n.s., not significant.

We investigated *SIGLEC9* expression at the single-cell level in our single-cell RNA-seq (scRNA-seq) dataset consisting of five patients with primary GBM (*24*), where we found *SIGLEC9* to be predominantly expressed by GAMs (Fig. 1B). This was also the case for other Siglec receptors (*SIGLEC1*, *CD22*, *SIGLEC7*, and *SIGLEC10*) (fig. S1D). Besides GAMs, we observed the expression of *CD22* and *SIGLEC10* in B cells and of *SIGLEC7* in NK cells, as previously reported by others (fig. S1D) (*19*, *25*, *26*). UDP-GlcNAc 2-epimerase/ManNAc kinase (*GNE*), a rate-limiting enzyme in the sialic acid biosynthesis pathway (*27*), was mainly expressed by GBM cells (Fig. 1B), as well as the sialyltransferase *ST3GAL4*, which has been identified as the main contributor to the synthesis of Siglec-9 ligands (fig. S1E) (*15*, *28*), suggesting the idea that there could be interactions between Siglec-9 in GAMs and sialic acid in GBM cells. Flow cytometry analysis of primary human GBM- and glioma-associated mouse MG revealed the high expression of Siglec-9 and Siglec-E protein, respectively (Fig. 1, C and D, and fig. S1, F and G). Up-regulation of Siglec-E was observed on mouse MG in the orthotopic tumor context (Fig. 1D). Staining of $CD45^{neg}$ cells in primary human GBM single-cell suspensions with recombinant Siglec-9 Fc chimeras to determine their sialic acid composition revealed a highly sialylated cell surface (Fig. 1E). Staining of different mouse glioma cell lines with recombinant Siglec-E Fc chimeras showed high sialylation in the mouse malignant astrocytoma cell line CT-2A (*29*) but not GL261 or the retrovirally induced primary mouse glioma cell line $PDGF^{+}Trp53^{-}$ (Fig. 1F) (*30*).

Inhibitory Siglec receptors on microglia reduce tumor cell phagocytosis

To investigate the role of Siglec–sialic acid signaling in regulating the MG-mediated antitumor immune response, we used an orthotopic GBM mouse model with MG-specific spatiotemporal deletion of *Siglece* by crossing $Siglece^{fl/fl}$ mice (*31*) with $Sall1^{CreERT2}$ mice (*32*) ($Siglece^{fl/fl} \times Sall1^{CreERT2}$). $Sall1^{CreERT2}$ mice harbor a tamoxifen-inducible Cre activity under transcriptional control of the *Sall1* promotor. *Sall1* represents an MG signature gene, not expressed by peripheral MdCs (*33*). We induced *Siglece* deletion by intraperitoneal (ip) tamoxifen injections beginning 7 days after inoculation of Luc2-tdTomato–labeled tumor cells and after confirmation of tumor engraftment by bioluminescence imaging (BLI) (Fig. 1G). We did not observe survival differences in CT-2A or GL261 tumor–bearing mice (Fig. 1H), despite the efficient deletion of Siglec-E in MG (Fig. 1, I and J, and fig. S1H). Nevertheless, flow cytometry analysis of the iTME unveiled high MG proliferation upon Siglec-E knockout (Fig. 1K), accompanied by an enhanced GBM cell uptake by the MG, measured as the percentage of $tdTomato^{+}$ MG (Fig. 1, L to N). The Siglec-E deletion–mediated prophagocytic effect in MG was more prominent in CT-2A tumor–bearing animals than in GL261-grafted mice (Fig. 1, M and N), probably because of the higher Siglec-E ligand expression on CT-2A than in GL261 cells (Fig. 1F). Intracellular uptake of tumor-derived tdTomato fluorescence by MG was microscopically confirmed using imaging flow cytometry (Fig. 1O and fig. S1I). Together, these results indicated that the inhibitory Siglec-E receptor plays a role in regulating MG-mediated tumor cell phagocytosis. However, perturbing Siglec-E signaling in MG was not sufficient to improve survival, leading us to comprehensively investigate differences between iTME in $Siglece^{fl/fl}$ and $Siglece^{fl/fl} \times Sall1^{CreERT2}$.

MG activation through Siglec-E deletion induces a counteracting, compensatory MdC response

Coexpression patterns of CD163 and CD86 in infiltrating MdCs (Fig. 2A) revealed an "M2-like" protumorigenic polarization shift in $Siglece^{fl/fl} \times Sall1^{CreERT2}$ mice in both the percentage of MdCs and the mean fluorescence intensity (MFI) (Fig. 2, B and C). Furthermore, we observed a counteracting up-regulation of Siglec-E in the total MdC population upon MG-specific Siglec-E deletion (Fig. 2D), which was particularly prevalent in the more abundant $CD163^{high}CD86^{low}$ M2-like MdCs (Fig. 2B). This compensatory up-regulation on MdCs was only observed for Siglec-E, whereas we did not measure expression changes in other Siglec receptors (fig. S2A).

Using scRNA-seq, we profiled the iTME from $Siglece^{fl/fl}$ and $Siglece^{fl/fl} \times Sall1^{CreERT2}$ CT-2A tumor–bearing mice (Fig. 2E), identifying 23 distinct cell clusters, including 7 GAM clusters, 10 lymphoid clusters, 1 NK cell cluster, 3 dendritic cell (DC) clusters, and 1 B cell cluster (Fig. 2F and fig. S2, B to D). Focusing on MG clusters (Fig. 2G), two clusters were identified (MG_1 and MG_2). A differential expression analysis between cells from $Siglece^{fl/fl}$ and $Siglece^{fl/fl} \times Sall1^{CreERT2}$ CT-2A tumor–bearing mice for these MG clusters revealed a partial reversal of a disease-associated MG (DAM) phenotype upon Siglec-E deletion (fig. S2E). DAMs were initially described in a genetic mouse model of Alzheimer's disease (*34*) but have been reported in other models of neurodegeneration and neuroinflammation (*35*, *36*), where excessive activation of MG proinflammatory functions may be detrimental and accelerate the disease (*37*). Upon Siglec-E deletion, we observed the down-regulation of DAM-signature genes (*37*), including tetraspanins (*Cd9*), chemokines (*Cxcl13*), and molecules involved in Trem2 signaling (*Lgals3*) and tissue remodeling (*Spp1* and *Gpnmb*). In contrast, genes involved in phagocytosis (*Axl* and *Arg1*) and cellular activation (*Trpm2*) were up-regulated (fig. S2E). Along the same line, gene set enrichment analysis (GSEA) on the differentially expressed genes (DEGs) using the MSigDB Hallmark collection (*38*) identified tumor necrosis factor–α (TNF-α) signaling through nuclear factor κB (NF-κB) to be up-regulated in Siglec-E–deleted MG (fig. S2F).

Focusing on MdCs (Fig. 2G; fig. S3, A to E; and data file S1), we identified two phenotypically distinct MdC clusters ($MdC\_Ly6c^{low}CD11c^{+}$ and $MdC\_Ly6c^{low}CD11c^{-}$), probably representing intermediate stages of differentiation toward monocyte-derived DCs and monocyte-derived macrophages, respectively (*39*, *40*). Among MdCs clusters, differential expression analysis attributed the highest number of DEGs to the $MdC\_Ly6c^{low}CD11c^{+}$ cluster [57 DEGs in $MdC\_Ly6c^{low}CD11c^{+}$, 12 DEGs in monocytes, 10 DEGs in $MdC\_Ly6c^{low}CD11c^{-}$, 12 DEGs in TAMs, and 10 DEGs in MdC_Proliferating, at a 5% false discovery rate (FDR); data file S2]. GSEA on the DEGs ascribed a highly immunosuppressive phenotype to these $MdC\_Ly6c^{low}CD11c^{+}$ cells upon MG-specific Siglec-E deletion, with down-regulation of genes modulating type I and type II interferon (IFN) responses and TNF-α signaling (Fig. 2H).

Using the same markers as in the scRNA-seq analysis, we identified the MdC subclusters by flow cytometry as well (fig. S3F). By applying this gating strategy, we noted that the increase of Siglec-E expression in the MdC compartment was not specific to one MdC subcluster (fig. S3G), but rather showed an increased coexpression pattern with CD163 among all MdCs (fig. S3, H and I). Therefore,

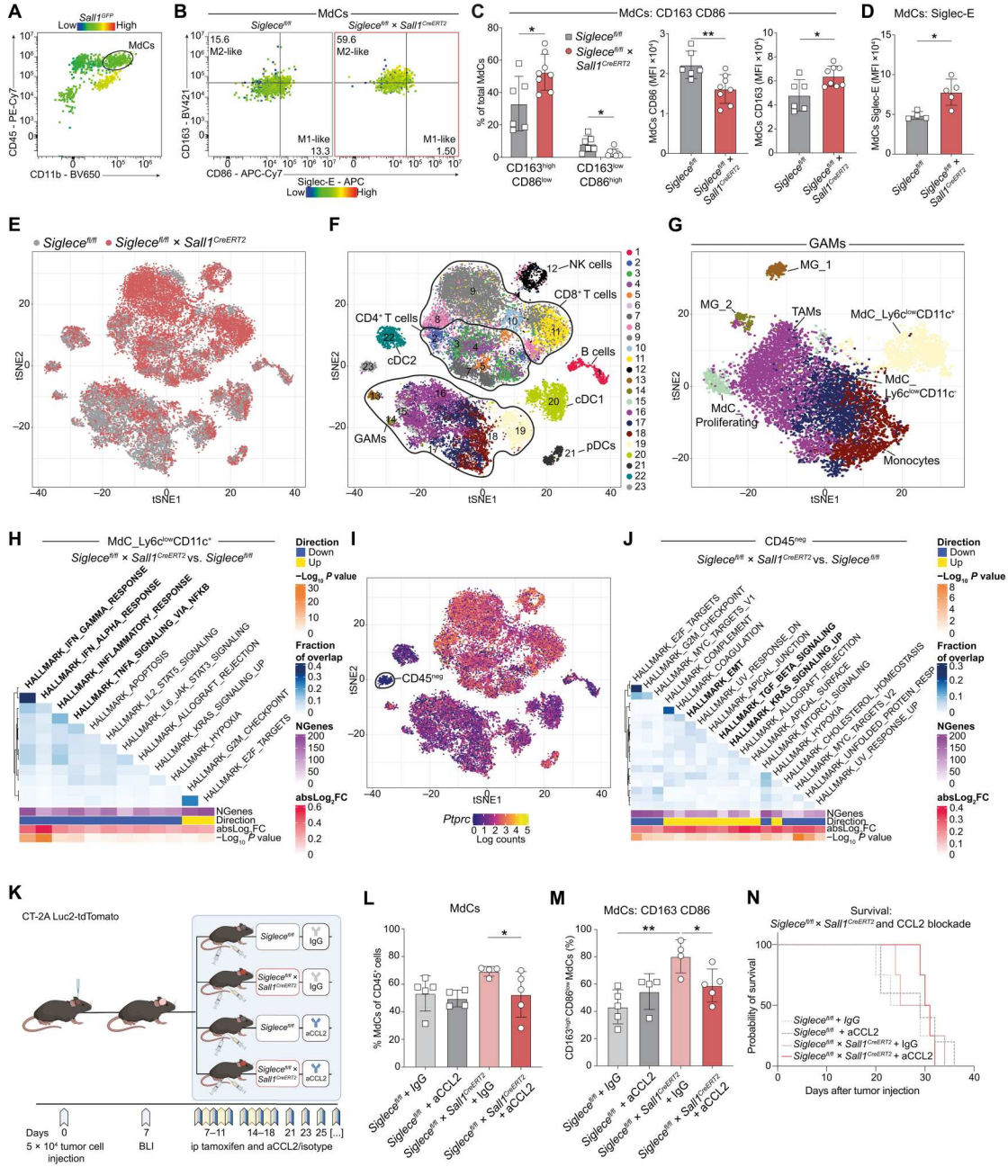

Fig. 2. MG activation through cell-specific Siglec-E deletion induces counteracting MdC responses. (**A** to **D**) Flow cytometry analysis of CD86 and CD163 expression on tumor-infiltrating MdCs, identified as $CD11b^{+}CD45^{high}$ events. (A) The gating strategy was confirmed in *Sall1*^{GFP} reporter mice. (B) Representative dot plots, overlaid with Siglec-E expression. APC, allophycocyanin. (C) Quantification of $CD163^{high}CD86^{low}$- and $CD163^{low}CD86^{high}$-coexpressing MdCs (left), MFI of CD86 on MdCs (middle), and MFI of CD163 on MdCs (right) (n = 6 to 8 mice per group). (D) Quantification of Siglec-E expression on MdCs (n = 4 or 5 mice per group). Results shown are from one experiment, representative of two independent experiments. (**E**) t-Distributed stochastic neighbor embedding (tSNE) plot from scRNA-seq analysis showing the distribution of sorted immune cells from *Siglece*$^{fl/fl}$ (gray) and *Siglece*$^{fl/fl}$ × *Sall1*^{CreERT2} (red) tumors. (**F**) tSNE plot showing the annotated cell populations. (**G**) tSNE plot of scRNA-seq analysis showing the subset of GAMs and their annotation. (**H**) Heatmap representation of GSEA results between $MdC\_Ly6c^{low}CD11c^{+}$ cells from *Siglece*$^{fl/fl}$ × *Sall1*^{CreERT2} and *Siglece*$^{fl/fl}$ tumors using the MSigDB Hallmark collection. The colors on the heatmap represent the fraction of overlap (Jaccard coefficient) between genes annotated to the gene sets. NGenes represents the size of the gene sets, and $absLog_2FC$ represents the average absolute $\log_2$ fold change of genes in the gene sets. (**I**) tSNE plot showing *Ptprc* (Cd45) expression across cells. Expression is shown as normalized $\log_2$ counts. (**J**) Heatmap representation of GSEA results between $CD45^{neg}$ cells from *Siglece*$^{fl/fl}$ × *Sall1*^{CreERT2} and *Siglece*$^{fl/fl}$ tumors, similar to (H). (**K**) Schematic of experimental design. (**L** to **N**) Flow cytometry analysis of tumor-infiltrating MdCs from *Siglece*$^{fl/fl}$ and *Siglece*$^{fl/fl}$ × *Sall1*^{CreERT2} CT-2A tumor–bearing mice treated with anti-CCL2 (aCCL2) or isotype control. Percentage of MdCs (L), percentage of $CD163^{high}CD86^{low}$-coexpressing MdCs (M), and survival (N) are shown for the treatment groups (n = 4 or 5 mice per group). The experiment was performed once. Data are presented as means ± SD and were analyzed using multiple unpaired Student's t test with Holm-Šidák's correction for multiple comparison test (C, left), unpaired two-tailed Student's t test (C, middle and right, and D), Kruskal-Wallis test with Dunn's multiple comparisons test (L) or one-way ANOVA with Šidák's correction for multiple comparison test (M). $^{*}P \leq 0.05$ and $^{**}P \leq 0.01$.

the increase in Siglec-E expression among MdCs is potentially caused by the increased infiltration of M2-like MdCs (Fig. 2C), indicating that Siglec-E might be associated with a protumorigenic phenotype in these cells.

In addition, differential abundance analysis revealed an increase in $CD8^+$ T cell cluster 9 ($CD8^+$ T cells_Pre-exhausted/Effector) in $Siglece^{fl/fl} \times Sall1^{CreERT2}$ mice (fig. S3, J and K). This corroborates the hypothesis that the infiltrating MdCs render the iTME protumorigenic. Although we focused our analysis on immune cells, we still captured transcripts originating from $CD45^{neg}$ cells (Fig. 2I), which acquired a progressive phenotype with up-regulation of genes involved in epithelial-mesenchymal transition (EMT), KRAS signaling, and increased transforming growth factor–β signaling after MG-specific Siglec-E deletion (Fig. 2J), which might facilitate the immunosuppressive shift of the MdC subcluster. Together, these data identified a population of early-phase MdCs as a main driver of the counteracting immunosuppressive response upon Siglec-E deletion–induced MG activation.

To test our hypothesis of early-phase MdCs as the main counteracting force to the antitumor MG response, we combined MG-specific Siglec-E deletion with C-C chemokine ligand 2 (CCL2) neutralization (Fig. 2K). This inhibits the recruitment of CCR2-expressing inflammatory monocytes to the tumor by retaining them in the bone marrow (*41*). Anti-CCL2 treatment led to less excessive infiltration of MdCs to the tumor site, mainly driven by a reduction of TAMs among MdCs (fig. S3L) and converted their M2-like polarization state upon concomitant MG-specific Siglec-E deletion. However, both treatments only restored the M2-like state to the same degree as the control (Fig. 2, L and M, and fig. S3L), indicating that recruitment of MdCs to the GBM iTME is a highly redundant mechanism that cannot be perturbed by antagonizing the action of a single tumor-attracting chemokine. Accordingly, the combination of MG-specific Siglec E deletion and anti-CCL2 treatment did not improve survival (Fig. 2N). These results showcase that MG-specific Siglec-E deletion promotes tumor cell phagocytosis, which is subsequently counteracted by infiltrating MdCs that acquire an immunosuppressive phenotype in the perturbed iTME.

Siglec-E deficiency in whole GAM population improves innate antitumor immunity

To test the role of inhibitory Siglec receptors on all GAMs, we used $Cx3cr1^{CreERT2}$ mice (*42*), which harbor tamoxifen-inducible Cre activity under transcriptional control of the C-X3-C motif chemokine receptor 1 (*Cx3cr1*) promoter. This allowed us to target both GAM populations in the GBM iTME (MG, as well as *Cx3cr1*-expressing MdCs) (Fig. 3A and fig. S4A). CT-2A–engrafted mice in the $Siglece^{fl/fl} \times Cx3cr1^{CreERT2}$ group showed a delayed tumor growth measured by in vivo BLI (Fig. 3, B and C, and fig. S4B) resulting in prolonged survival compared with $Siglece^{fl/fl}$ and $Cx3cr1^{CreERT2}$ control mice (Fig. 3D). Flow cytometry–based immune profiling revealed increased MG- and MdC-mediated tumor cell phagocytosis by dual MG- and MdC-specific Siglec-E deletion (Fig. 3, E and F), accompanied by the increased production of TNF-α (Fig. 3F). In addition, MG displayed accentuated antigen presentation capacity with increased surface major histocompatibility complex II (MHC-II) and costimulatory CD86 expression upon *Cx3cr1*-specific Siglec-E deletion. The induction of an M2-like polarization of MdCs that we observed in $Siglece^{fl/fl} \times Sall1^{CreERT2}$ (Fig. 2, B and C) was abolished in $Siglece^{fl/fl} \times Cx3cr1^{CreERT2}$ mice (fig. S4C). However, the MdC compartment showed no difference in CD86 and MHC-II expression (Fig. 3F). The proportion of intratumoral MdCs was comparable between cohorts at an endpoint, indicating that recruitment of these cells to the tumor site remained intact in *Cx3cr1*-specific Siglec-E–deleted mice (fig. S4D). MdCs were the dominant $CD45^+$ cell population at the endpoint (fig. S4D), highlighting the potent myeloid influx during CT-2A tumor progression. Applying the flow cytometry–based MdC subcluster analysis (Fig. 3G), we were able to identify the same populations as seen by scRNAseq in the $Siglece^{fl/fl} \times Sall1^{CreERT2}$ model (Fig. 2G and fig. S3F). Although we did not observe any difference in MdC subcluster frequency between $Siglece^{fl/fl}$ and $Siglece^{fl/fl} \times Cx3cr1^{CreERT2}$ mice (fig. S4E), we identified TAMs to be the main phagocytic subpopulation upon Siglec-E deletion (Fig. 3H), which was accompanied by the greatest decrease in Siglec-E expression (by both percentage and MFI) in TAMs compared with other MdC subpopulations (fig. S4F). To test Siglec-E deletion in an additional model, we used the mouse glioma stem cell (GSC) line 005 (*43*). 005 GSC–derived brain tumors have been shown to share characteristics with human GBM, including heterogeneous stem cell–like properties and invasiveness (*43*), and to resemble more closely the immune-phenotypic signature than CT-2A (*44*). On the other hand, we found only a moderate sialylation, with around 30% of cells expressing Siglec-E ligands (fig. S4G). Using $Siglece^{fl/fl} \times Cx3cr1^{CreERT2}$ mice engrafted with 005 GSC–derived tumors (fig. S4H), we recapitulated the main findings of the CT-2A model, including prolonged survival upon GAM-specific Siglec-E deletion and increased tumor phagocytosis (fig. S4, I and J).

Siglec-E–deficient MdCs show increased antigen cross-presentation and T cell cross-priming capacity

Within tumor-infiltrating lymphocytes, we observed mainly a $CD8^+$ T cell–driven response upon GAM-specific Siglec-E deletion with increased activation signature ($CD69^+Ki\text{-}67^+$ coexpression) and effector cytokine IFN-γ production (Fig. 4, A and B). Together with the absent MHC-II response in MdCs after increased tumor cell phagocytosis, we hypothesized that loss of Siglec-E on MdCs could enhance antigen cross-presentation and cross-priming of $CD8^+$ T cells. Therefore, we pulsed the $CD11b^+$ GAM fraction isolated from mice on day 15 after tumor inoculation with ovalbumin protein ex vivo (Fig. 4C) and evaluated the presence of MHC-I–bound ovalbumin-derived peptide SIINFEKL. We noted an increase in antigen cross-presentation by MdCs, but not MG, upon Siglec-E deletion (Fig. 4D). MdC subclustering by flow cytometry revealed TAMs to display the most differential SIINFEKL/H-$2K^b$ staining among MdCs (fig. S5, A and B). To estimate the antigen-presenting capacity of MdCs and MG individually upon Siglec-E deletion, we sorted tumor-associated MdCs and MG 15 days after tumor injection and cocultured them with naive $CD8^+$ OT-I or $CD4^+$ OT-II T cells, respectively (Fig. 4E). This resulted in increased OT-1 T cell activation in an antigen-specific manner by MdCs from $Siglece^{fl/fl} \times Cx3cr1^{CreERT2}$ mice compared with $Siglece^{fl/fl}$ control (Fig. 4F). Siglec-E–deleted MG only moderately increased $CD4^+$ T cell activation (Fig. 4G), which might explain the lack of a differential $CD4^+$ T cell response (Fig. 4B). In addition, we observed a reduced number of MG in the tumor-bearing hemisphere compared with the non–tumor-bearing hemisphere, especially at later disease stages (fig. S5, C and D). It has been shown that MG are more prominent in the tumor periphery and less within the

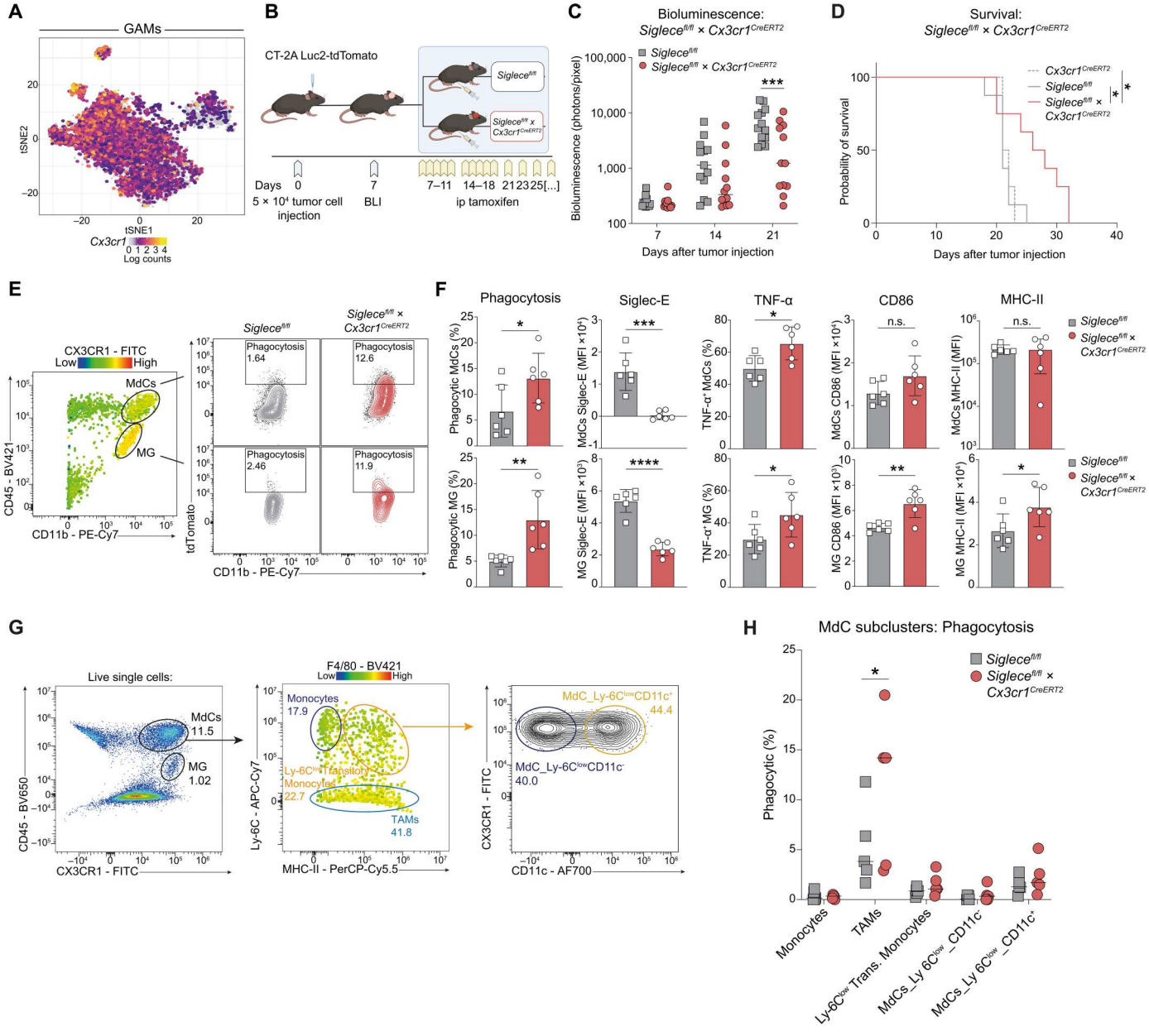

Fig. 3. GAM-specific Siglec-E deletion boosts innate antitumor immunity. (**A**) tSNE plot of scRNA-seq analysis showing *Cx3cr1* expression in the GAM clusters subset. Expression is shown as normalized $\log_2$ counts. (**B**) Schematic of experimental design. (**C**) Surrogate tumor growth assessed by BLI between *Siglece*$^{fl/fl}$ and *Siglece*$^{fl/fl}$ × *Cx3cr1*^{CreERT2} CT-2A tumor–bearing animals (n = 12 or 13 mice per group). (**D**) Survival of *Cx3cr1*^{CreERT2}, *Siglece*$^{fl/fl}$, and *Siglece*$^{fl/fl}$ × *Cx3cr1*^{CreERT2} CT-2A tumor–bearing animals (n = 8 mice per group, except n = 4 mice in the *Cx3cr1*^{CreERT2} group). Results were pooled from two independent experiments. (**E** and **F**) Flow cytometry analysis of MdCs (top row) and MG (bottom row) from *Siglece*$^{fl/fl}$ and *Siglece*$^{fl/fl}$ × *Cx3cr1*^{CreERT2} CT-2A tumor–bearing mice. Representative contour plots showing tumor cell phagocytosis assessed by tdTomato$^+$ MdCs and MG (E) and bar graphs showing quantified phagocytosis as well as expression of Siglec-E, TNF-α, CD86, and MHC-II within MdCs (top row) and MG (bottom row) upon GAM-specific Siglec-E deletion and respective Cre-negative littermate controls (F) (n = 6 mice per group). Results shown are from one experiment, representative of two independent experiments. (**G** and **H**) Flow cytometry analysis of MdC subclusters as identified by scRNA-seq (Fig. 2G) from *Siglece*$^{fl/fl}$ and *Siglece*$^{fl/fl}$ × *Cx3cr1*^{CreERT2} CT-2A tumor–bearing mice. Representative gating strategy (G) and quantification of phagocytic MdC subpopulations (H) (n = 5 mice per group). FITC, fluorescein isothiocyanate; PerCP, peridinin chlorophyll protein; AF, Alexa Fluor; Trans., transitory. Results were pooled from two independent experiments. Data are presented as median (C and H) or means ± SD (F) and were analyzed by two-way ANOVA with Šidák's correction for multiple comparison test (C and H), log-rank Mantel-Cox test (D), or unpaired two-tailed Student's t test (F). *$P \leq 0.05$, **$P \leq 0.01$, ***$P \leq 0.001$, and ****$P \leq 0.0001$.

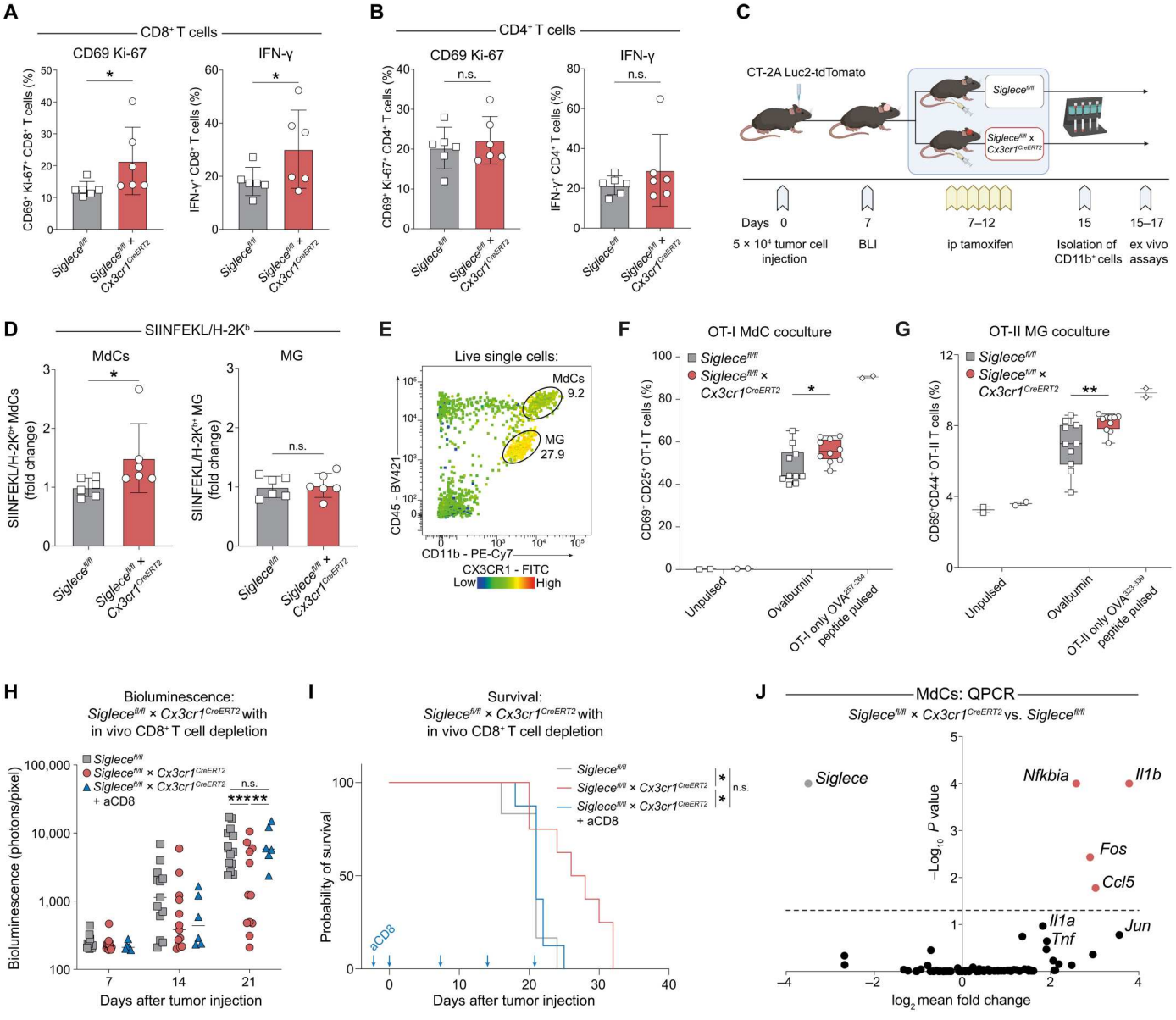

Fig. 4. Intratumoral Siglec-E–deleted MdCs show increased antigen cross-presentation and T cell cross-priming capacity ex vivo. (**A** and **B**) Flow cytometry analysis of CD69 and Ki-67 coexpression (left) and intracellular IFN-γ production (right) in tumor-infiltrating $CD8^+$ (A) and $CD4^+$ T cells (B) from *Siglece*$^{fl/fl}$ and *Siglece*$^{fl/fl}$ × *Cx3cr1*^{CreERT2} CT-2A tumor–bearing animals ($n = 6$ mice per group). Results shown are from one experiment, representative of two independent experiments. (**C**) Schematic of experimental design to magnetically enrich for tumor-associated $CD11b^+$ cells used in (**D**). (D) Flow cytometry analysis of SIINFEKL peptide bound to H-$2K^b$ on MdCs (left) and MG (right) ($n = 6$ mice per group). Results were pooled from two independent experiments. (**E**) Sorting strategy to individually isolate tumor-associated MdCs and MG used in (**F**) and (**G**) at day 15 after tumor injection. (F and G) Flow cytometry analysis of $CD69^+CD25^+$ OT-I T cells (F) and $CD69^+CD44^+$ OT-II T cells (G) after a 24-hour coculture with unpulsed or ovalbumin-pulsed MdCs or MG, respectively ($n = 10$ mice per genotype). T cell–only peptide-pulsed condition serves as a positive control for T cell activation. Results were pooled from two independent experiments. (**H** and **I**) BLI as surrogate for tumor growth ($n = 6$ to 13 mice per group) (H) and survival ($n = 6$ to 8 mice per group) (I) of in vivo $CD8^+$ T cell–depleted *Siglece*$^{fl/fl}$ × *Cx3cr1*^{CreERT2} CT-2A tumor–bearing animals, compared with animals from Fig. 3 (C and D). The blue arrows in (I) indicate anti-mouse CD8a intraperitoneal administrations (days −2, 0, 7, 14, and 21). Results shown are from one experiment, representative of two independent experiments. (**J**) QPCR analysis of NF-κB target genes in MdCs sorted from *Siglece*$^{fl/fl}$ and *Siglece*$^{fl/fl}$ × *Cx3cr1*^{CreERT2} CT-2A tumor–bearing mice on day 15 after tumor cell injection and 8 days after induction of GAM-specific Siglec-E deletion ($n = 9$ or 10 mice per group). Results were pooled from three independent experiments, with $n = 3$ or 4 mice pooled per genotype each. QPCR analysis of *Siglece* was done separately, $n = 4$ mice per genotype. Data are presented as means ± SD (A, B, and D), box plots (F and G), or median (H). Data were analyzed using unpaired Student's *t* test (A and B), two-tailed Mann-Whitney test (D), one-way ANOVA with Šidák's correction for multiple comparison test (F and G), two-way ANOVA with Šidák's correction for multiple comparison test (H), log-rank Mantel-Cox test (I), two-way ANOVA for NF-κB target genes, or unpaired two-tailed Student's *t* test for *Siglece* (J). $*P \leq 0.05$, $**P \leq 0.01$, and $***P \leq 0.001$.

tumor bulk (*45*) and, therefore, might contribute less to the antitumor immunity, which represents a limitation of orthotopic tumor implantation models. To further argue for the predominant role of Siglec-E–deleted MdCs in this model, we used *Siglece*$^{fl/fl}$ × *Lyz2*^{Cre} mice (also known as *Lysm*^{Cre}) to target MdCs alone (fig. S5E). MdC-restricted Siglec-E deletion (fig. S5F) was sufficient to delay tumor growth, although survival was not improved (fig. S5, G and H). To experimentally test the contribution of the MdC-CD8$^+$ T cell axis as observed in the ex vivo coculture assay, we depleted CD8$^+$ T cells in vivo using an anti-CD8 antibody that reversed the survival advantage gained by GAM Siglec-E deletion (Fig. 4, H and I).

Efficient priming of CD8$^+$ T cells and promoting their effector functions require both antigen cross-presentation and secretion of pro-inflammatory cytokines by MdCs (*46*). To identify activated pathways downstream of Siglec-E deletion, we conducted an unbiased proteomic analysis of sorted, tumor-associated MdCs and compared the list of differentially expressed proteins with the Kyoto Encyclopedia of Genes and Genomes pathway database (*47*). This revealed the overrepresentation of proteins also involved in the interleukin-17 (IL-17) signaling pathway in Siglec-E–deleted compared with wild-type MdCs (fig. S5I). IL-17 is known to trigger the activation of the canonical NF-κB cascade and subsequently up-regulates the expression of various pro-inflammatory genes (*48*). To test the hypothesis that, similar to the activation of the IL-17 pathway, loss of Siglec-E in MdCs might induce expression of NF-κB target genes, we profiled signature genes within the NF-κB signaling pathway in tumor-associated MdCs 15 days after tumor engraftment by quantitative real-time PCR (QPCR). This revealed increased expression of pro-inflammatory genes (*Il1b* and *Ccl5*) and genes associated with the activator protein 1 transcription-complex (AP-1) (*Fos*) in MdCs from *Siglece*$^{fl/fl}$ × *Cx3cr1*^{CreERT2} mice versus *Siglece*$^{fl/fl}$ animals (Fig. 4J and fig. S5J). Increased NF-κB signaling induced negative feedback circuits by increased expression of *Nfkbia*, which is one of the earliest genes induced after NF-κB activation leading to termination of NF-κB signaling (*49*). Collectively, these findings indicate that GAM-specific Siglec-E deletion promotes tumor cell phagocytosis by MG and MdCs, enhances intratumoral CD8$^+$ T cell responses by antigen cross-presentation, and increases the production of pro-inflammatory cytokines by MdCs, potentially mediated by NF-κB signaling axis.

Genetic targeting of sialic acid on CT-2A cells recapitulates the main findings of GAM-specific Siglec-E deletion in vivo

To complement the effect of immune evasion mediated by the Siglec-E receptor, we targeted its sialic acid ligands on CT-2A cells by knocking out the GNE enzyme (CT-2A$^{\Delta GNE}$) (Fig. 5A and fig. S6A). CT-2A$^{\Delta GNE}$ cells showed no differences with regard to their in vitro proliferation and viability compared to the wild-type control (CT-2A^{WT}) (fig. S6B). Orthotopic transplantation of CT-2A$^{\Delta GNE}$ cells into C57BL/6 mice resulted in prolonged survival and increased tumor cell phagocytosis, TNF-α production, and MG-expressed MHC-II (Fig. 5, B to E), recapitulating the main findings from *Siglece*$^{fl/fl}$ × *Cx3cr1*^{CreERT2} mice. When applying the flow cytometry–based MdC subclustering, we similarly identified the TAM subcluster as the main responsive cell type upon disruption of the Siglec–sialic acid axis, with increased infiltration, TNF-α production, and phagocytosis (the latter in the MHC-II^{low} TAM subpopulation) (fig. S6, C to E). To validate the role of Siglec-E as the main receptor for tumor sialylation, we assessed the survival of CT-2A^{WT}– and CT-2A$^{\Delta GNE}$–injected *Siglece*$^{fl/fl}$ and *Siglece*$^{fl/fl}$ × *Cx3cr1*^{CreERT2} mice. Whereas the survival of CT-2A$^{\Delta GNE}$–injected *Siglece*$^{fl/fl}$ mice was superior compared with CT-2A^{WT} tumors, no difference in survival between CT-2A^{WT} and CT-2A$^{\Delta GNE}$ tumors was observed in *Siglece*$^{fl/fl}$ × *Cx3cr1*^{CreERT2} mice (Fig. 5F). This indicates that the therapeutic effects of desialylation in vivo are largely dependent on functional Siglec-E expression in the innate immune compartment, which is in accordance with previous findings (*50*, *51*). Although we observed a favorable CD4$^+$ T cell response with less CD25$^+$Foxp3$^+$ T$_{regs}$ and more Cxcr3$^+$T-bet$^+$ T helper 1 CD4$^+$ T cells in CT-2A$^{\Delta GNE}$ tumor-bearing animals at endpoint (fig. S6F), the main driver of the adaptive immune response after innate immune activation was CD8$^+$ T cells. This was exemplified by less abundant programmed cell death protein 1 (PD-1)$^+$, T cell Ig and mucin domain-containing protein 3 (TIM-3)$^+$, lymphocyte activation gene 3 (LAG-3)$^+$, and cytotoxic T lymphocyte–associated protein 4 (CTLA-4)$^+$–coexpressing CD8$^+$ T cells; greater degranulation capacity; and increased IFN-γ production in CT-2A$^{\Delta GNE}$ tumor-bearing animals (Fig. 5, G and H). Together, targeting Siglec receptor ligands in the tumor recapitulates the main findings of GAM-specific Siglec-E deletion in the host.

GAM-specific Siglec-E deletion improves survival of anti-CD47 and anti–PD-1 cotreated animals

To harness and further elucidate the therapeutic potential of GAM-specific Siglec-E deletion (*Siglece*$^{fl/fl}$ × *Cx3cr1*^{CreERT2}), we initiated combination treatments with CD47 blockade (Fig. 6A), an established innate immunotherapeutic agent (*8*–*10*). It has been previously shown that CD47 blockade enhances tumor cell phagocytosis and T cell cross-priming (*52*). We observed a reduction in tumor growth (Fig. 6B) and one of nine animals showing tumor rejection in the combinatorial condition (Fig. 6C). In *Siglece*$^{fl/fl}$ × *Cx3cr1*^{CreERT2} tumors collected at endpoint, tumor-infiltrating CD8$^+$ T cells demonstrated high PD-1 expression (Fig. 6D), and programmed cell death ligand 1 (PD-L1) was up-regulated on CD45^{neg} and CD45^{pos} cells (Fig. 6E). This compensatory T cell checkpoint up-regulation could be caused by increased CD8$^+$ T cell activation and IFN-γ production after GAM-specific Siglec-E deletion (Fig. 4A) (*53*). To overcome this potential resistance mechanism, we additionally treated tumor-bearing *Siglece*$^{fl/fl}$ × *Cx3cr1*^{CreERT2} mice with both CD47 and PD-1 blocking antibodies (Fig. 6, F to H), which showed prolonged survival compared with *Siglece*$^{fl/fl}$ mice receiving anti-CD47 and anti–PD-1 treatment (Fig. 6H). Although we did not observe an improved initial tumor control in the triple-therapy–treated animals compared to *Siglece*$^{fl/fl}$ × *Cx3cr1*^{CreERT2} + anti-CD47 (Fig. 6, G and H, and fig. S7), we identified complete tumor rejection in 3 of 13 of animals (Fig. 6H). Contralateral hemisphere tumor-rechallenging of surviving animals in the triple-treatment cohort led again to tumor rejection, whereas GAM–Siglec-E–deleted/anti-CD47–treated mice succumbed to tumor progression after rechallenge (Fig. 6I). Together, these data suggest that, by targeting both innate and adaptive immune checkpoints, a lasting immunological memory can be achieved.

Siglec-E/9 blockade induces immune responses and antitumor activity in mice and in human GBM explants

To determine the translational potential of Siglec-E blockade, we implanted osmotic minipumps with brain infusion catheters to continuously infuse Siglec-E blocking or IgG control antibodies

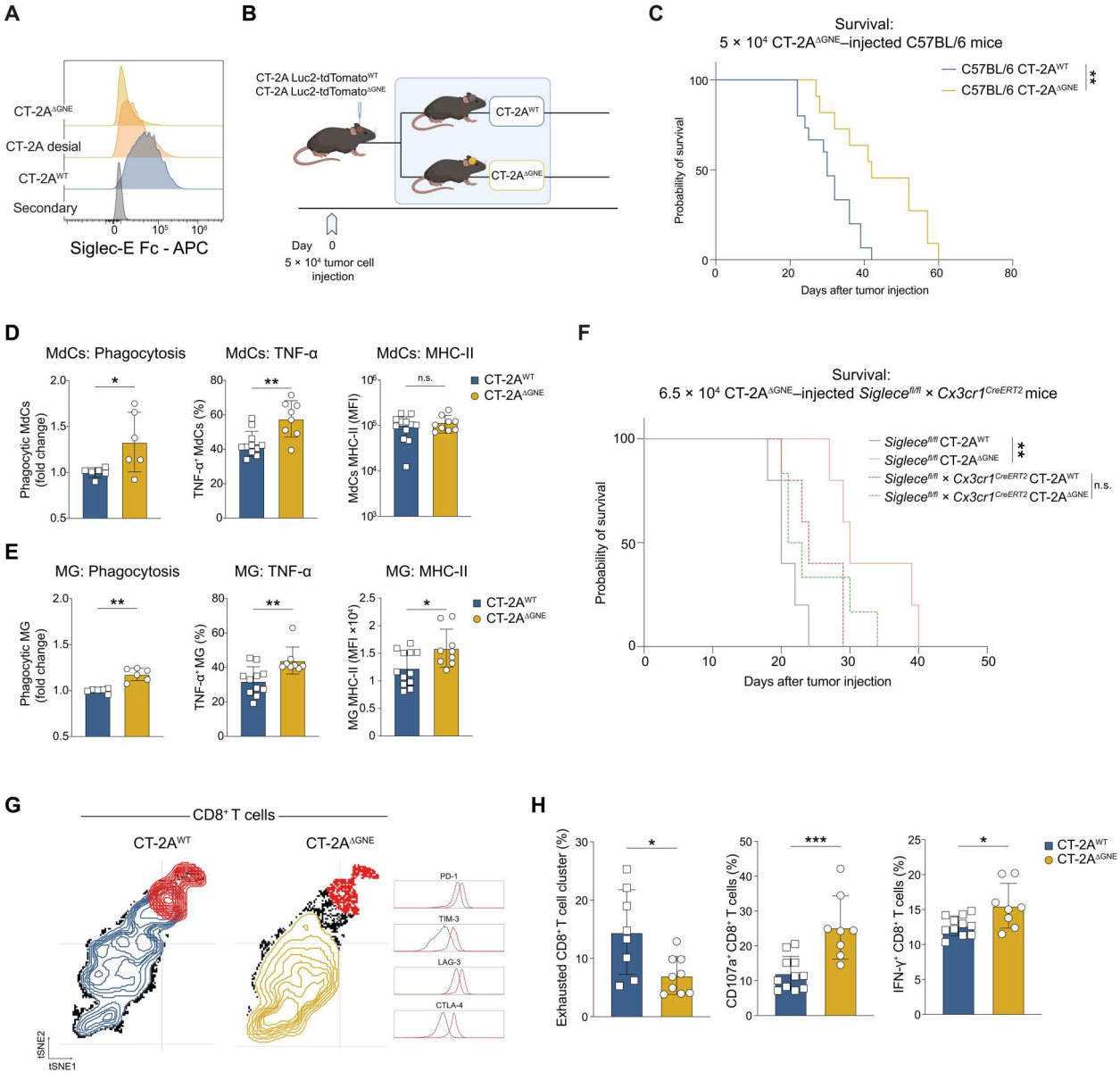

Fig. 5. Genetic targeting of sialic acid on CT-2A cells phenocopies Siglec-E deletion in the host. (**A**) Representative histogram of Siglec-E Fc staining on CT-2A^{WT}, enzymatically desialylated (desial) CT-2A, and CT-2A$^{\Delta GNE}$ cells. (**B**) Schematic of experimental design. (**C**) Survival of CT-2A^{WT}– and CT-2A$^{\Delta GNE}$–injected C57BL/6 wild-type mice (n = 11 to 15 mice per group). Results were pooled from two independent experiments. (**D** and **E**) Flow cytometry analysis of phagocytosis, TNF-α expression, and MHC-II expression on MdCs (D) and MG (E) from CT-2A^{WT}– and CT-2A$^{\Delta GNE}$–injected C57BL/6 wild-type mice (n = 6 mice per group for phagocytosis, n = 8 to 11 mice per group for other analyses). Results were pooled from two independent experiments. (**F**) Survival of CT-2A^{WT}– and CT-2A$^{\Delta GNE}$–injected *Siglece*$^{fl/fl}$ and *Siglece*$^{fl/fl}$ × *Cx3cr1*^{CreERT2} mice (n = 5 or 6 mice per group). Results are from one experiment. (**G**) Flow cytometry analysis of inhibitory T cell receptors on intratumoral CD8$^+$ T cells visualized on tSNE map (tSNE maps show concatenated CD8$^+$ T cells from n = 8 mice per group). Red cluster marks exhausted CD8$^+$ T cells identified by high coexpression of inhibitory receptors (PD-1, TIM-3, LAG-3, and CTLA-4), indicated by histograms. Red histogram marks median marker expression in red cluster (exhausted CD8$^+$ T cell cluster), and black dotted histogram indicates median marker expression in the remaining cells. (**H**) Quantification of flow cytometry analysis, showing percentage of exhausted CD8$^+$ T cells (PD-1^{high}, TIM-3^{high}, LAG-3^{high}, and CTLA-4^{high}) (left), CD107a$^+$ (middle), and IFN-γ$^+$ (right) intratumoral CD8$^+$ T cells between CT-2A^{WT}– and CT-2A$^{\Delta GNE}$–injected C57BL/6 wild-type mice (n = 8 to 11 mice per group). Results were pooled from two independent experiments. Data are presented as means ± SD and were analyzed by unpaired two-tailed Student's t test (D and H), two-tailed Mann-Whitney test (E), or log-rank Mantel-Cox test (C and F). *$P \leq 0.05$, **$P \leq 0.01$, and ***$P \leq 0.001$.

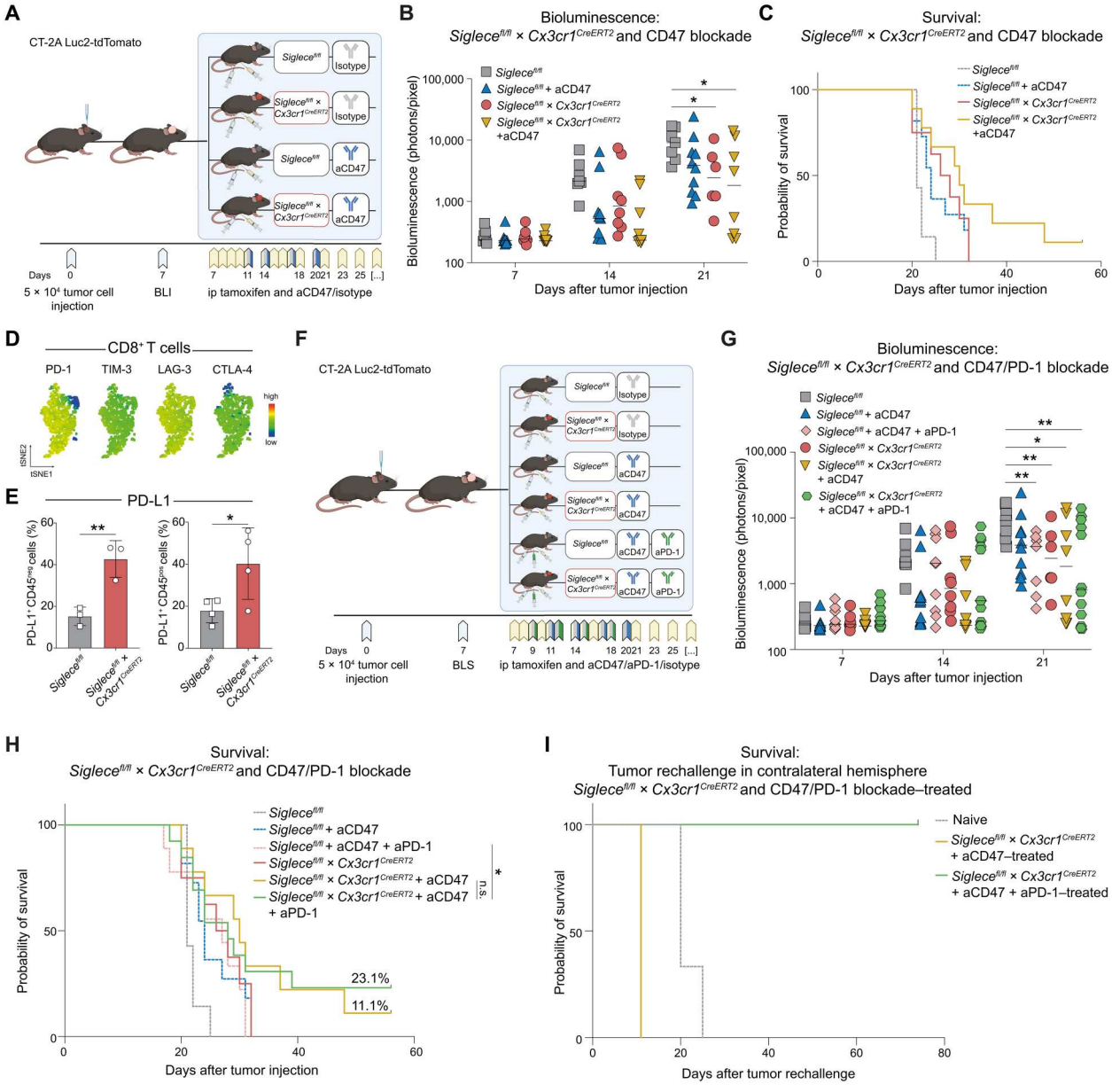

Fig. 6. Siglec-E deletion boosts GBM immunotherapy. (**A**) Schematic of experimental design. (**B** and **C**) Surrogate tumor growth assessed by BLI (B) and survival ($n = 7$ to 11 mice per group) (C) of *Siglece*$^{fl/fl}$ and *Siglece*$^{fl/fl}$ × *Cx3cr1*^{CreERT2} CT-2A tumor-bearing animals treated with anti-CD47 or isotype control. Results were pooled from two independent experiments. (**D**) Flow cytometry analysis of inhibitory T cell receptors on intratumoral CD8$^+$ T cells shown on tSNE map (tSNE maps show concatenated CD8$^+$ T cells from $n = 6$ mice per group). (**E**) Flow cytometry analysis of PD-L1 expression on CD45^{neg} (left) and CD45^{pos} cells (right) from of *Siglece*$^{fl/fl}$ and *Siglece*$^{fl/fl}$ × *Cx3cr1*^{CreERT2} mice ($n = 3$ or 4 mice per group). (**F**) Schematic of experimental design. (**G** and **H**) Surrogate tumor growth assessed by BLI (G) and survival ($n = 7$ to 13 mice per group) (H) of *Siglece*$^{fl/fl}$ and *Siglece*$^{fl/fl}$ × *Cx3cr1*^{CreERT2} CT-2A tumor–bearing animals treated with anti-CD47 and anti–PD-1 (aPD-1) or isotype control. Results were pooled from two independent experiments. (**I**) Rechallenge of the tumor-free mice from (C) and (H) and tumor-naive control mice with intracranial injection of 5×10^4 CT-2A tumor cells into the contralateral hemisphere ($n = 1$ for *Siglece*$^{fl/fl}$ × *Cx3cr1*^{CreERT2} + aCD47 treated, $n = 3$ mice per group for other two groups). Data are presented as median (B and G) or means ± SD (E) and were analyzed by two-way ANOVA with Holm-Šidák's correction for multiple comparison test (B and G), unpaired two-tailed Student's *t* test (E), or RMST comparison (C and H). *$P \leq 0.05$ and **$P \leq 0.01$.

into the tumor parenchyma of glioma-bearing mice (Fig. 7A and fig. S8A). After randomization into the respective treatment groups according to bioluminescence count on day 6 after tumor injection, we observed delayed tumor growth in the intervention group on day 14 after tumor injection (6 days after pump implantation) (fig. S8B). Flow cytometry analysis revealed increased phagocytosis and TNF-α production by MG in the anti–Siglec-E–treated mice, whereas no difference among MdC subclusters was observed (fig. S8, C and D). However, other innate immune cells previously not targeted by the genetic *Siglece*$^{fl/fl}$ × *Cx3cr1*^{CreERT2} model like Cx3cr1$^-$CD11c$^+$ DCs (fig. S8E) displayed increased tumor cell phagocytosis (fig. S8F). Ultimately, this contributed to

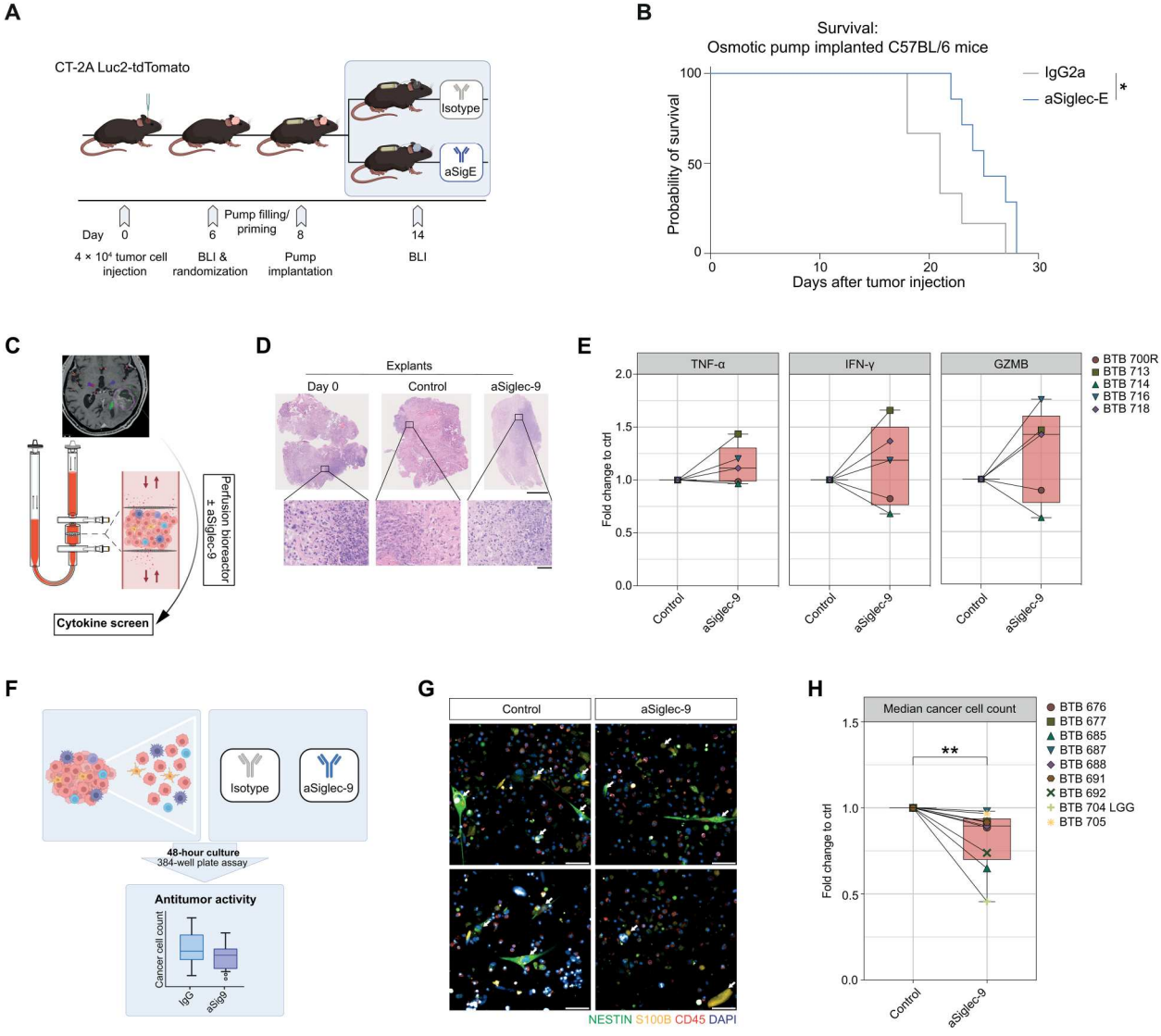

Fig. 7. Siglec-9 blockade induces immune response and antitumor activity in mice and in human GBM explants. (**A**) Schematic of experimental design. (**B**) Survival ($n = 6$ or 7 mice per group) of C57BL/6 CT-2A tumor–bearing animals treated with anti–Siglec-E or isotype control antibody intracranially delivered by implanted osmotic minipumps. (**C**) Schematic of experimental design. Fresh tumor biopsies were taken and directly transferred into 3D perfusion bioreactors. Explants were cultured for 5 days in the presence or absence of anti–Siglec-9 blocking antibody. Soluble proteins from bioreactor media were measured by PEA to assess response per patient sample. (**D**) Representative hematoxylin and eosin–stained images of formalin-fixed paraffin-embedded explants on the day of tumor resection (day 0) and after 5 days of culture in perfusion bioreactors. Scale bars, 1000 μm (overview) and 50 μm (close-up). (**E**) Fold change in TNF-α, IFN-γ, and GZMB secretion measured in the media of anti–Siglec-9–treated versus control bioreactors, for each individual patient. (**F**) Schematic of experimental design. Glioma samples ($n = 9$) were dissociated and cultured for 48 hours in the presence of Siglec-9 blocking antibody or isotype control. (**G**) Representative immunofluorescence images of one patient sample (BTB 688) treated with isotype (left) or anti–Siglec-9 (right). White arrows denote cancer cells. Scale bars, 50 μm. (**H**) Fold change in median cancer cell count in anti–Siglec-9–treated versus control. Per patient, six technical replicates for control and three technical replicates for anti–Siglec-9 samples (fig. S8H). The median of technical replicates is used and plotted as fold change. Data were analyzed using log-rank Mantel-Cox test (B) or Wilcoxon signed-rank test (H). *$P \leq 0.05$ and **$P \leq 0.01$. DAPI, 4′,6-diamidino-2-phenylindole.

the prolonged survival of the anti–Siglec-E–treated animals (Fig. 7B). Next, we prospectively collected GBM specimens from four primary and one recurrent GBM patient undergoing neurosurgical resection. All samples were neuropathologically diagnosed as GBM grade 4, *Isocitrate Dehydrogenase 1/2* (*IDH*) wild type (table S1). Intact tumor fragments (explants) were subsequently cultured in three-dimensional (3D) perfusion bioreactors for 5 days in the presence or absence of Siglec-9 blocking antibody (Fig. 7C) (*54*). As previously reported by our group, this culture system provides a flow of the media through the tissue, enabling culturing intact tissue of greater thickness and thereby better preserving the GBM iTME compared with static conditions (Fig. 7D) (*55*).

An analysis of secreted soluble proteins by highly sensitive proximity extension assay (PEA) technology after 5 days in culture identified three out of five patients (60%) as responders to Siglec-9 blockade, as indicated by a signature of induced TNF-α, IFN-γ, and granzyme B (GZMB) expression (Fig. 7E). One of the nonresponders was the patient with recurrent GBM (BTB 700R).

Within the responders, the observed increase was significant ($P < 0.05$) for IFN-γ and GZMB (fig. S8G).

Next, we assessed the antitumor activity of Siglec-9 blockade–induced immune activation on a single-cell level. Single-cell suspensions from nine additional patients with newly diagnosed glioma (eight GBM, grade 4, *IDH* wild type, and one LGG; table S1) were exposed to Siglec-9 blocking antibody or control for 48 hours (Fig. 7F). Using an automated image-based screening platform (*56*) to read out $S100B^+CD45^-$ or $NESTIN^+CD45^-$ glioma cell counts (Fig. 7G), Siglec-9 disruption efficiently reduced the number of glioma cells despite interpatient heterogeneity (Fig. 7H and fig. S8H).

DISCUSSION

Here, we identified the Siglec-sialic acid axis as an innate immune inhibitory pathway in GBM mediating an immunosuppressive iTME. We demonstrate that the deletion of Siglec receptors on MG and MdCs or reduction of Siglec ligands on tumor cells can reverse this immune suppression, allowing successful combinatorial immunotherapy in preclinical models. As the main mechanism, we show that Siglec-E deletion leads to increased tumor cell phagocytosis by MG and MdC, mainly TAMs, and elevated expression of NF-κB target genes in MdCs. This mediates cross-priming of $CD8^+$ T cells (fig. S9) and, when combined with other cancer immunotherapies, conveyed a survival benefit in an aggressive and poorly immunogenic CT-2A GBM preclinical model (*44*).

Previous preclinical studies have shown similar antiphagocytic (*17*, *57*–*59*) and macrophage differentiating properties (*15*, *16*, *60*) for Siglec receptors in cancer and other diseases. Our study expands this knowledge on the interactions of Siglec receptors with sialoglycans by dissecting the interplay between the two main innate immune populations in the GBM iTME. We found a counteracting MdC response upon Siglec-E deletion-driven MG activation and proliferation. Yeo and colleagues (*61*) recently reported similar changes in their study investigating longitudinal changes in the immune cell composition throughout tumor progression in a genetic mouse GBM model. Specifically, they identified a highly proliferating population of GBM-associated MG, for which the authors discussed a decisive role in activating emergency myelopoiesis in GBM and recruiting bone marrow–derived immunosuppressive myeloid cells to the GBM iTME (*61*). This paralleled our observation of a Siglec-E deletion–induced activation and proliferation of MG cells, and the counteracting ingress of immunosuppressive MdCs, which could only be reverted to the frequency observed in control animals by CCL2 inhibition. Although the tumor cells were not the primary focus of our scRNA-seq analysis after MG Siglec-E disruption, we found changes in the CT-2A transcriptome as well, particularly concerning EMT pathways. This might unveil further tumor cell–intrinsic plasticity and resistance mechanisms upon perturbance of iTME components such as MG and highlights potential paracrine and intercellular reactions between neoplastic cells and MG induced by selective deletion of Siglec-E.

By extending the cell type–specific Siglec-E deletion to the MdC compartment, we observed increased antitumor immunity and up-regulation of NF-κB target genes. Others similarly attributed a role as a negative modulator of NF-κB activity to Siglec-9 (*58*, *62*). In our RNA validation data, *Ccl5* was among the highest up-regulated NF-κB target genes upon MdC-specific Siglec-E deletion. Several studies showed positive correlations between the expression of inflammatory chemokine *CCL5* and immune cell recruitment to the tumor (*63*–*65*). However, some controversy arose regarding the role of CCL5 in cancer, because other studies suggested that CCL5 has potential tumor-promoting effects by either directly affecting tumor growth by expanding cancer stem cells (*66*) or promoting immune escape by stabilizing PD-L1 (*67*). Unlike IFN-γ, which enhances PD-L1 expression at the transcriptional level (*53*), CCL5 has been shown to modulate the deubiquitination and stability of PD-L1 (*67*). This might contribute to the adaptive resistance after Siglec-E deletion and illustrates the complex relationship between innate and adaptive immune responses.

Our data highlight the Siglec–sialic acid axis as an attractive therapeutic target in patients with GBM. Together with recent findings, our study further underlines the importance of combining innate and adaptive immunotherapies, especially in less immunogenic and ICI-resistant tumors, such as GBM (*52*). Using combined immunotherapy, we noted the separation of "responding" and "nonresponding" animals as early as day 14 after tumor injection. This highlights the need for future characterization of the nonresponding tumor cell subsets to tailor treatments. One possible approach in this direction was recently pursued by Zemek *et al.* (*68*) where they identified the temporally restricted activity of IFN-β within inflammatory monocytes to underlie the response to combined immune checkpoint therapy. By targeting IFN-β in a time-dependent manner, they were able to improve the response rate to combined immune checkpoint blockade.

Targeting sialic acids as ligands for Siglec receptors on tumor cells represents an alternative approach to therapeutically disrupting the Siglec–sialic acid pathway, as demonstrated by genetically targeting sialic acid biosynthesis in CT-2A cells. By applying this strategy, concerns regarding functional redundancy and potential compensatory mechanisms after the blockade of one Siglec receptor would be mitigated. In line with this, recent work showcased the high efficacy of tumor cell desialylation (*17*, *50*, *51*, *59*, *69*). However, even a targeted approach, for example, by using antibody-sialidase conjugates (*51*), would most likely cause severe adverse events, given that sialic acid participates as an integral part of ganglioside structure in synaptogenesis and neural transmission (*70*). Additional work will be needed to identify GBM cell–specific sialylation patterns enabling cancer cell–targeted desialylation therapies.

No difference in phagocytosis upon antibody-mediated Siglec-E blockade was observed among MdCs, specifically TAMs. This could be caused by the intracranial delivery method, which might target primarily peri-tumoral MG, rather than bone marrow–derived TAMs, which are dispersed inside the tumor bulk and enriched in the perivascular area (*45*). Therefore, more animal studies are needed to determine the most efficient route of administration, time point, and dosage to target all relevant immune populations. Using cultured, perfused 3D tumor explants [as recently described by our group (*55*)] and an image-based ex vivo drug screening platform, we showcased the translational relevance of Siglec-9 disruption within GBM. We observed the biggest decrease in tumor cell count after Siglec-9 blockade in the patient with LGG, and considering the TCGA survival data, further studies on the role of Siglec receptors in LGG are needed.

A limitation of our study is that we did not resolve the mechanisms leading to immunological memory after combined anti-CD47 and anti–PD-1 treatment in the subset of GAM–Siglec-E–deficient responding animals. The exact contribution, as well as the temporal aspects of each individual immunotherapeutic agent, remains unclear. It will be of considerable interest to dissect the host response upon Siglec-E/9 disruption in combination with immunotherapeutic agents in a time-dependent manner in different mouse models (syngeneic, xenograft, and viral induction) and patient explants to pinpoint conserved response mechanisms. Whereas our study provides functional data for the TAM subset to be the main responsive population upon Siglec-E deletion, it does not resolve its origin, transcriptional regulation, and particularly its recruitment into the iTME. Recent studies advanced our understanding in this regard: first, by identifying the skull and vertebral bone marrow as myeloid cell reservoirs for the CNS parenchyma (*71*); second, by describing differentiation programs in the monocyte-to-phagocyte transition (*72*); and, third, dissecting transcriptional clusters within inflammatory macrophages (*73*). It will be of considerable interest in future studies to investigate how these mechanisms might be perturbed during tumorigenesis and specifically upon Siglec-E deletion, giving rise to new combinatorial interventions.

Together, we showed that loss of inhibitory Siglec receptors promotes glioma-associated MG and mainly TAMs among MdCs to phagocytize GBM cells and improve cross-presentation and subsequent T cell activation. Using a poorly immunogenic GBM preclinical model, we demonstrated the therapeutic potential of combined Siglec-E blockade with ICI against GBM to facilitate innate and adaptive antitumor immune responses. Furthermore, we demonstrated the translational potential of Siglec-9 blockade–induced immune activation in patient-derived explant cultures, paving the way to local therapy regimens. These results build on a growing interest in designing combination immunotherapies with innate and adaptive ICI and underscore the value of Siglec blockade in liberating innate immune responses to potentiate antitumor immunity.

MATERIALS AND METHODS

Study design

The experiments were focused on deciphering the role of Siglec-E in mediating an immunosuppressive iTME in GBM and the functional consequences of perturbing Siglec-E signaling in MG and later in MdCs. The immunocompetent murine studies were complemented by in vitro experiments using primary human tumor material to confirm findings in a human setting. Human adult GBM tissue samples were obtained from the Neurosurgical Clinic of University Hospital of Basel, Switzerland, in accordance with the Swiss Human Research Act and institutional ethics committee (EKNZ 02019-02358). All patients gave written informed consent for tumor biopsy collection and signed a declaration permitting the use of their biopsy specimens in scientific research, including storage in our brain tumor biobank (Req-2019-00553). All patient-identifying information was removed, and tissues were coded for identification. Patient characteristics from all participating patients are listed in table S1. We used flow cytometry, scRNA-seq, proteomics, in vivo depletion studies, bioreactor cultures, and automated microscopy to identify treatment responses. For most animal experiments, randomization was not possible because the comparison point was mouse genotype. Mice of different treatment groups were cohoused in the same cage to blind experimenters in determining the humane endpoint. No power analyses were used to predetermine sample sizes in mouse experiments. However, sample sizes were chosen on the basis of prior literature using similar experimental paradigms. The *n* values and particular statistical methods are indicated in the figure legends and in the "Statistical analysis" section.

Statistical analysis

scRNA-seq and proteomic statistical analysis were completed as described in the Supplementary Materials. All other statistical analyses were performed using GraphPad Prism (GraphPad Software v.9.4.0). Raw, individual-level data are presented in data file S3. The number of experimental replicates and the number of independent experiments and statistical tests used are given in the figure legends. In general, for normally distributed datasets, as assessed by Shapiro-Wilk or D'Agostino-Pearson's test, we used an unpaired two-tailed Student's *t* test when two groups were compared. For comparing more than two groups, a one-way analysis of variance (ANOVA) was applied. When variables were not normally distributed, we used the nonparametric Mann-Whitney or Kruskal-Wallis test. For comparing a quantitative variable between two groups, two-way ANOVA was used, followed by Šidák's post hoc corrections for multiple comparisons. Survival data were analyzed using the log-rank Mantel-Cox test or restricted mean survival time (RMST). RMST analysis was used to account for the presence of censoring. The calculations were performed in R using the survRM2 package. We used max τ (largest observed time in each of the two groups), and the differences in RMST between subgroups were calculated as 95% confidence intervals with *P* values. $P < 0.05$ was considered statistically significant. Data collection and analysis were not performed blind to the conditions of the experiments. Outliers were removed using GraphPad Outlier Calculator, which uses the Grubbs' test (www.graphpad.com/quickcalcs/Grubbs1.cfm). This was the case for Fig. 6 (C and H), where we excluded a survival outlier in the *Siglece*$^{fl/fl}$ group. All graphical illustrations were created with BioRender.com.

Supplementary Materials

This PDF file includes:
Materials and Methods
Figs. S1 to S9
Tables S1 to S3
References (*74–100*)

Other Supplementary Material for this manuscript includes the following:
Data files S1 to S3
MDAR Reproducibility Checklist

View/request a protocol for this paper from *Bio-protocol*.

REFERENCES AND NOTES

1. M. Weller, M. van den Bent, M. Preusser, E. Le Rhun, J. C. Tonn, G. Minniti, M. Bendszus, C. Balana, O. Chinot, L. Dirven, P. French, M. E. Hegi, A. S. Jakola, M. Platten, P. Roth, R. Rudà, S. Short, M. Smits, M. J. B. Taphoorn, A. von Deimling, M. Westphal, R. Soffietti, G. Reifenberger, W. Wick, EANO guidelines on the diagnosis and treatment of diffuse gliomas of adulthood. *Nat. Rev. Clin. Oncol.* **18**, 170–186 (2021).
2. S. L. Topalian, C. G. Drake, D. M. Pardoll, Immune checkpoint blockade: A common denominator approach to cancer therapy. *Cancer Cell* **27**, 450–461 (2015).

3. D. A. Reardon, A. A. Brandes, A. Omuro, P. Mulholland, M. Lim, A. Wick, J. Baehring, M. S. Ahluwalia, P. Roth, O. Bähr, S. Phuphanich, J. M. Sepulveda, P. De Souza, S. Sahebjam, M. Carleton, K. Tatsuoka, C. Taitt, R. Zwirtes, J. Sampson, M. Weller, Effect of nivolumab vs bevacizumab in patients with recurrent glioblastoma: The CheckMate 143 phase 3 randomized clinical trial. *JAMA Oncol.* **6**, 1003–1010 (2020).
4. M. Lim, M. Weller, A. Idbaih, J. Steinbach, G. Finocchiaro, R. R. Raval, G. Ansstas, J. Baehring, J. W. Taylor, J. Honnorat, K. Petrecca, F. De Vos, A. Wick, A. Sumrall, S. Sahebjam, I. K. Mellinghoff, M. Kinoshita, M. Roberts, R. Slepetis, D. Warad, D. Leung, M. Lee, D. A. Reardon, A. Omuro, Phase III trial of chemoradiotherapy with temozolomide plus nivolumab or placebo for newly diagnosed glioblastoma with methylated MGMT promoter. *Neuro Oncol.* **24**, 1935–1949 (2022).
5. A. Omuro, A. A. Brandes, A. F. Carpentier, A. Idbaih, D. A. Reardon, T. Cloughesy, A. Sumrall, J. Baehring, M. van den Bent, O. Bähr, G. Lombardi, P. Mulholland, G. Tabatabai, U. Lassen, J. M. Sepulveda, M. Khasraw, E. Vauleon, Y. Muragaki, A. M. Di Giacomo, N. Butowski, P. Roth, X. Qian, A. Z. Fu, Y. Liu, V. Potter, A. G. Chalamandaris, K. Tatsuoka, M. Lim, M. Weller, Radiotherapy combined with nivolumab or temozolomide for newly diagnosed glioblastoma with unmethylated MGMT promoter: An international randomized phase 3 trial. *Neuro Oncol.* **25**, 123–134 (2022).
6. F. Klemm, R. R. Maas, R. L. Bowman, M. Kornete, K. Soukup, S. Nassiri, J. P. Brouland, C. A. Iacobuzio-Donahue, C. Brennan, V. Tabar, P. H. Gutin, R. T. Daniel, M. E. Hegi, J. A. Joyce, Interrogation of the microenvironmental landscape in brain tumors reveals disease-specific alterations of immune cells. *Cell* **181**, 1643–1660.e17 (2020).
7. E. Friebel, K. Kapolou, S. Unger, N. G. Núñez, S. Utz, E. J. Rushing, L. Regli, M. Weller, M. Greter, S. Tugues, M. C. Neidert, B. Becher, Single-cell mapping of human brain cancer reveals tumor-specific instruction of tissue-invading leukocytes. *Cell* **181**, 1626–1642.e20 (2020).
8. S. Gholamin, S. S. Mitra, A. H. Feroze, J. Liu, S. A. Kahn, M. Zhang, R. Esparza, C. Richard, V. Ramaswamy, M. Remke, A. K. Volkmer, S. Willingham, A. Ponnuswami, A. McCarty, P. Lovelace, T. A. Storm, S. Schubert, G. Hutter, C. Narayanan, P. Chu, E. H. Raabe, G. T. Harsh, M. D. Taylor, M. Monje, Y. J. Cho, R. Majeti, J. P. Volkmer, P. G. Fisher, G. Grant, G. K. Steinberg, H. Vogel, M. Edwards, I. L. Weissman, S. H. Cheshier, Disrupting the CD47-SIRPα anti-phagocytic axis by a humanized anti-CD47 antibody is an efficacious treatment for malignant pediatric brain tumors. *Sci. Transl. Med.* **9**, eaaf2968 (2017).
9. G. Hutter, J. Theruvath, C. M. Graef, M. Zhang, M. K. Schoen, E. M. Manz, M. L. Bennett, A. Olson, T. D. Azad, R. Sinha, C. Chan, S. Assad Kahn, S. Gholamin, C. Wilson, G. Grant, J. He, I. L. Weissman, S. S. Mitra, S. H. Cheshier, Microglia are effector cells of CD47-SIRPα antiphagocytic axis disruption against glioblastoma. *Proc. Natl. Acad. Sci. U.S.A.* **116**, 997–1006 (2019).
10. M. Zhang, G. Hutter, S. A. Kahn, T. D. Azad, S. Gholamin, C. Y. Xu, J. Liu, A. S. Achrol, C. Richard, P. Sommerkamp, M. K. Schoen, M. N. McCracken, R. Majeti, I. Weissman, S. S. Mitra, S. H. Cheshier, Anti-CD47 treatment stimulates phagocytosis of glioblastoma by M1 and M2 polarized macrophages and promotes M1 polarized macrophages in vivo. *PLOS ONE* **11**, e0153550 (2016).
11. S. S. Pinho, C. A. Reis, Glycosylation in cancer: Mechanisms and clinical implications. *Nat. Rev. Cancer* **15**, 540–555 (2015).
12. M. J. Schultz, A. F. Swindall, S. L. Bellis, Regulation of the metastatic cell phenotype by sialylated glycans. *Cancer Metastasis Rev.* **31**, 501–518 (2012).
13. O. M. Pearce, H. Laubli, Sialic acids in cancer biology and immunity. *Glycobiology* **26**, 111–128 (2016).
14. L. Veillon, C. Fakih, H. Abou-El-Hassan, F. Kobeissy, Y. Mechref, Glycosylation changes in brain cancer. *ACS Chem. Neurosci.* **9**, 51–72 (2018).
15. E. Rodriguez, K. Boelaars, K. Brown, R. J. Eveline Li, L. Kruijssen, S. C. M. Bruijns, T. van Ee, S. T. T. Schetters, M. H. W. Crommentuijn, J. C. van der Horst, N. C. T. van Grieken, S. J. van Vliet, G. Kazemier, E. Giovannetti, J. J. Garcia-Vallejo, Y. van Kooyk, Sialic acids in pancreatic cancer cells drive tumour-associated macrophage differentiation via the Siglec receptors Siglec-7 and Siglec-9. *Nat. Commun.* **12**, 1270 (2021).
16. R. Beatson, V. Tajadura-Ortega, D. Achkova, G. Picco, T. D. Tsourouktsoglou, S. Klausing, M. Hillier, J. Maher, T. Noll, P. R. Crocker, J. Taylor-Papadimitriou, J. M. Burchell, The mucin MUC1 modulates the tumor immunological microenvironment through engagement of the lectin Siglec-9. *Nat. Immunol.* **17**, 1273–1281 (2016).
17. A. A. Barkal, R. E. Brewer, M. Markovic, M. Kowarsky, S. A. Barkal, B. W. Zaro, V. Krishnan, J. Hatakeyama, O. Dorigo, L. J. Barkal, I. L. Weissman, CD24 signalling through macrophage Siglec-10 is a target for cancer immunotherapy. *Nature* **572**, 392–396 (2019).
18. H. Laubli, O. M. Pearce, F. Schwarz, S. S. Siddiqui, L. Deng, M. A. Stanczak, L. Deng, A. Verhagen, P. Secrest, C. Lusk, A. G. Schwartz, N. M. Varki, J. D. Bui, A. Varki, Engagement of myelomonocytic Siglecs by tumor-associated ligands modulates the innate immune response to cancer. *Proc. Natl. Acad. Sci. U.S.A.* **111**, 14211–14216 (2014).
19. J. E. Hudak, S. M. Canham, C. R. Bertozzi, Glycocalyx engineering reveals a Siglec-based mechanism for NK cell immunoevasion. *Nat. Chem. Biol.* **10**, 69–75 (2014).
20. M. Perdicchio, L. A. Cornelissen, I. Streng-Ouwehand, S. Engels, M. I. Verstege, L. Boon, D. Geerts, Y. van Kooyk, W. W. Unger, Tumor sialylation impedes T cell mediated anti-tumor responses while promoting tumor associated-regulatory T cells. *Oncotarget* **7**, 8771–8782 (2016).
21. M. Perdicchio, J. M. Ilarregui, M. I. Verstege, L. A. M. Cornelissen, S. T. T. Schetters, S. Engels, M. Ambrosini, H. Kalay, H. Veninga, J. M. M. den Haan, L. A. van Berkel, J. N. Samsom, P. R. Crocker, T. Sparwasser, L. Berod, J. J. Garcia-Vallejo, Y. van Kooyk, W. W. J. Unger, Sialic acid-modified antigens impose tolerance via inhibition of T-cell proliferation and de novo induction of regulatory T cells. *Proc. Natl. Acad. Sci. U.S.A.* **113**, 3329–3334 (2016).
22. R. L. Bowman, Q. Wang, A. Carro, R. G. W. Verhaak, M. Squatrito, GlioVis data portal for visualization and analysis of brain tumor expression datasets. *Neuro Oncol.* **19**, 139–141 (2017).
23. The Cancer Genome Atlas Research Network, Comprehensive, integrative genomic analysis of diffuse lower-grade gliomas. *N. Engl. J. Med.* **372**, 2481–2498 (2015).
24. P. Schmassmann, J. Roux, S. Dettling, S. Hogan, T. Shekarian, T. A. Martins, M.-F. Ritz, S. Herter, M. Bacac, G. Hutter, Single-cell characterization of human GBM reveals regional differences in tumor-infiltrating leukocyte activation. *bioRxiv*, 2022.06.17.496574 (2022).
25. J. Müller, I. Obermeier, M. Wöhner, C. Brandl, S. Mrotzek, S. Angermüller, P. C. Maity, M. Reth, L. Nitschke, CD22 ligand-binding and signaling domains reciprocally regulate B-cell Ca^{2+} signaling. *Proc. Natl. Acad. Sci. U.S.A.* **110**, 12402–12407 (2013).
26. G.-Y. Chen, N. K. Brown, P. Zheng, Y. Liu, Siglec-G/10 in self-nonself discrimination of innate and adaptive immunity. *Glycobiology* **24**, 800–806 (2014).
27. S. Hinderlich, W. Weidemann, T. Yardeni, R. Horstkorte, M. Huizing, UDP-GlcNAc 2-epimerase/ManNAc kinase (GNE): A master regulator of sialic acid synthesis. *Top. Curr. Chem.* **366**, 97–137 (2015).
28. C. Büll, R. Nason, L. Sun, J. Van Coillie, D. Madriz Sørensen, S. J. Moons, Z. Yang, S. Arbitman, S. M. Fernandes, S. Furukawa, R. McBride, C. M. Nycholat, G. J. Adema, J. C. Paulson, R. L. Schnaar, T. J. Boltje, H. Clausen, Y. Narimatsu, Probing the binding specificities of human Siglecs by cell-based glycan arrays. *Proc. Natl. Acad. Sci. U.S.A.* **118**, e2026102118 (2021).
29. T. N. Seyfried, M. el-Abbadi, M. L. Roy, Ganglioside distribution in murine neural tumors. *Mol. Chem. Neuropathol.* **17**, 147–167 (1992).
30. C. Giachino, J.-L. Boulay, R. Ivanek, A. Alvarado, C. Tostado, S. Lugert, J. Tchorz, M. Coban, L. Mariani, B. Bettler, J. Lathia, S. Frank, S. Pfister, M. Kool, V. Taylor, A tumor suppressor function for notch signaling in forebrain tumor subtypes. *Cancer Cell* **28**, 730–742 (2015).
31. J. Wang, M. Manni, A. Bärenwaldt, R. Wieboldt, N. Kirchhammer, R. Ivanek, M. Stanczak, A. Zippelius, D. König, N. Rodrigues Manutano, H. Läubli, Siglec receptors modulate dendritic cell activation and antigen presentation to T cells in cancer. *Front. Cell Dev. Biol.* **10**, 828916 (2022).
32. S. Inoue, M. Inoue, S. Fujimura, R. Nishinakamura, A mouse line expressing Sall1-driven inducible Cre recombinase in the kidney mesenchyme. *Genesis* **48**, 207–212 (2010).
33. A. Buttgereit, I. Lelios, X. Yu, M. Vrohlings, N. R. Krakoski, E. L. Gautier, R. Nishinakamura, B. Becher, M. Greter, Sall1 is a transcriptional regulator defining microglia identity and function. *Nat. Immunol.* **17**, 1397–1406 (2016).
34. H. Keren-Shaul, A. Spinrad, A. Weiner, O. Matcovitch-Natan, R. Dvir-Szternfeld, T. K. Ulland, E. David, K. Baruch, D. Lara-Astaiso, B. Toth, S. Itzkovitz, M. Colonna, M. Schwartz, I. Amit, A unique microglia type associated with restricting development of Alzheimer's disease. *Cell* **169**, 1276–1290.e17 (2017).
35. D. V. Hansen, J. E. Hanson, M. Sheng, Microglia in Alzheimer's disease. *J. Cell Biol.* **217**, 459–472 (2017).
36. B. A. Friedman, K. Srinivasan, G. Ayalon, W. J. Meilandt, H. Lin, M. A. Huntley, Y. Cao, S.-H. Lee, P. C. G. Haddick, H. Ngu, Z. Modrusan, J. L. Larson, J. S. Kaminker, M. P. van der Brug, D. V. Hansen, Diverse brain myeloid expression profiles reveal distinct microglial activation states and aspects of Alzheimer's disease not evident in mouse models. *Cell Rep.* **22**, 832–847 (2018).
37. Y. Chen, M. Colonna, Microglia in Alzheimer's disease at single-cell level. Are there common patterns in humans and mice? *J. Exp. Med.* **218**, e20202717 (2021).
38. A. Liberzon, C. Birger, H. Thorvaldsdottir, M. Ghandi, J. P. Mesirov, P. Tamayo, The molecular signatures database (MSigDB) hallmark gene set collection. *Cell Syst* **1**, 417–425 (2015).
39. G. T. Belz, S. L. Nutt, Transcriptional programming of the dendritic cell network. *Nat. Rev. Immunol.* **12**, 101–113 (2012).
40. G. Agliardi, A. R. Liuzzi, A. Hotblack, D. De Feo, N. Núñez, C. L. Stowe, E. Friebel, F. Nannini, L. Rindlisbacher, T. A. Roberts, R. Ramasawmy, I. P. Williams, B. M. Siow, M. F. Lythgoe, T. L. Kalber, S. A. Quezada, M. A. Pule, S. Tugues, K. Straathof, B. Becher, Intratumoral IL-12 delivery empowers CAR-T cell immunotherapy in a pre-clinical model of glioblastoma. *Nat. Commun.* **12**, 444 (2021).

41. B.-Z. Qian, J. Li, H. Zhang, T. Kitamura, J. Zhang, L. R. Campion, E. A. Kaiser, L. A. Snyder, J. W. Pollard, CCL2 recruits inflammatory monocytes to facilitate breast-tumour metastasis. *Nature* **475**, 222–225 (2011).
42. C. N. Parkhurst, G. Yang, I. Ninan, J. N. Savas, J. R. Yates, J. J. Lafaille, B. L. Hempstead, D. R. Littman, W.-B. Gan, Microglia promote learning-dependent synapse formation through brain-derived neurotrophic factor. *Cell* **155**, 1596–1609 (2013).
43. T. Marumoto, A. Tashiro, D. Friedmann-Morvinski, M. Scadeng, Y. Soda, F. H. Gage, I. M. Verma, Development of a novel mouse glioma model using lentiviral vectors. *Nat. Med.* **15**, 110–116 (2009).
44. J. K. Khalsa, N. Cheng, J. Keegan, A. Chaudry, J. Driver, W. L. Bi, J. Lederer, K. Shah, Immune phenotyping of diverse syngeneic murine brain tumors identifies immunologically distinct types. *Nat. Commun.* **11**, 3912 (2020).
45. A. Buonfiglioli, D. Hambardzumyan, Macrophages and microglia: The cerberus of glioblastoma. *Acta Neuropathol. Commun.* **9**, 54 (2021).
46. J. M. Curtsinger, M. F. Mescher, Inflammatory cytokines as a third signal for T cell activation. *Curr. Opin. Immunol.* **22**, 333–340 (2010).
47. M. Kanehisa, S. Goto, KEGG: Kyoto encyclopedia of genes and genomes. *Nucleic Acids Res.* **28**, 27–30 (2000).
48. M. J. McGeachy, D. J. Cua, S. L. Gaffen, The IL-17 family of cytokines in health and disease. *Immunity* **50**, 892–906 (2019).
49. J. A. Prescott, J. P. Mitchell, S. J. Cook, Inhibitory feedback control of NF-κB signalling in health and disease. *Biochem. J.* **478**, 2619–2664 (2021).
50. M. A. Gray, M. A. Stanczak, N. R. Mantuano, H. Xiao, J. F. A. Pijnenborg, S. A. Malaker, C. L. Miller, P. A. Weidenbacher, J. T. Tanzo, G. Ahn, E. C. Woods, H. Läubli, C. R. Bertozzi, Targeted glycan degradation potentiates the anticancer immune response in vivo. *Nat. Chem. Biol.* **16**, 1376–1384 (2020).
51. M. A. Stanczak, N. Rodrigues Mantuano, N. Kirchhammer, D. E. Sanin, F. Jacob, R. Coelho, A. V. Everest-Dass, J. Wang, M. P. Trefny, G. Monaco, A. Bärenwaldt, M. A. Gray, A. Petrone, A. S. Kashyap, K. Glatz, B. Kasenda, K. Normington, J. Broderick, L. Peng, O. M. T. Pearce, E. L. Pearce, C. R. Bertozzi, A. Zippelius, H. Läubli, Targeting cancer glycosylation repolarizes tumor-associated macrophages allowing effective immune checkpoint blockade. *Sci. Transl. Med.* **14**, eabj1270 (2022).
52. C. A. von Roemeling, Y. Wang, Y. Qie, H. Yuan, H. Zhao, X. Liu, Z. Yang, M. Yang, W. Deng, K. A. Bruno, C. K. Chan, A. S. Lee, S. S. Rosenfeld, K. Yun, A. J. Johnson, D. A. Mitchell, W. Jiang, B. Y. S. Kim, Therapeutic modulation of phagocytosis in glioblastoma can activate both innate and adaptive antitumour immunity. *Nat. Commun.* **11**, 1508 (2020).
53. A. Garcia-Diaz, D. S. Shin, B. H. Moreno, J. Saco, H. Escuin-Ordinas, G. A. Rodriguez, J. M. Zaretsky, L. Sun, W. Hugo, X. Wang, G. Parisi, C. P. Saus, D. Y. Torrejon, T. G. Graeber, B. Comin-Anduix, S. Hu-Lieskovan, R. Damoiseaux, R. S. Lo, A. Ribas, Interferon receptor signaling pathways regulating PD-L1 and PD-L2 expression. *Cell Rep.* **19**, 1189–1201 (2017).
54. A. F. Carlin, S. Uchiyama, Y. C. Chang, A. L. Lewis, V. Nizet, A. Varki, Molecular mimicry of host sialylated glycans allows a bacterial pathogen to engage neutrophil Siglec-9 and dampen the innate immune response. *Blood* **113**, 3333–3336 (2009).
55. T. Shekarian, C. P. Zinner, E. M. Bartoszek, W. Duchemin, A. T. Wachnowicz, S. Hogan, M. M. Etter, J. Flammer, C. Paganetti, T. A. Martins, P. Schmassmann, S. Zanganeh, F. Le Goff, M. G. Muraro, M.-F. Ritz, D. Phillips, S. S. Bhate, G. L. Barlow, G. P. Nolan, C. M. Schürch, G. Hutter, Immunotherapy of glioblastoma explants induces interferon-γ responses and spatial immune cell rearrangements in tumor center, but not periphery. *Sci. Adv.* **8**, eabn9440 (2022).
56. B. Snijder, G. I. Vladimer, N. Krall, K. Miura, A.-S. Schmolke, C. Kornauth, O. Lopez de la Fuente, H.-S. Choi, E. van der Kouwe, S. Gültekin, L. Kazianka, J. W. Bigenzahn, G. Hoermann, N. Prutsch, O. Merkel, A. Ringler, M. Sabler, G. Jeryczynski, M. E. Mayerhoefer, I. Simonitsch-Klupp, K. Ocko, F. Felberbauer, L. Müllauer, G. W. Prager, B. Korkmaz, L. Kenner, W. R. Sperr, R. Kralovics, H. Gisslinger, P. Valent, S. Kubicek, U. Jäger, P. B. Staber, G. Superti-Furga, Image-based ex-vivo drug screening for patients with aggressive haematological malignancies: Interim results from a single-arm, open-label, pilot study. *Lancet Haematol.* **4**, e595–e606 (2017).
57. J. V. Pluvinage, M. S. Haney, B. A. H. Smith, J. Sun, T. Iram, L. Bonanno, L. Li, D. P. Lee, D. W. Morgens, A. C. Yang, S. R. Shuken, D. Gate, M. Scott, P. Khatri, J. Luo, C. R. Bertozzi, M. C. Bassik, T. Wyss-Coray, CD22 blockade restores homeostatic microglial phagocytosis in ageing brains. *Nature* **568**, 187–192 (2019).
58. C. S. Delaveris, S. H. Chiu, N. M. Riley, C. R. Bertozzi, Modulation of immune cell reactivity with *cis*-binding Siglec agonists. *Proc. Natl. Acad. Sci.* **118**, e2012408118 (2021).
59. J. Theruvath, M. Menard, B. A. H. Smith, M. H. Linde, G. L. Coles, G. N. Dalton, W. Wu, L. Kiru, A. Delaidelli, E. Sotillo, J. L. Silberstein, A. C. Geraghty, A. Banuelos, M. T. Radosevich, S. Dhingra, S. Heitzeneder, A. Tousley, J. Lattin, P. Xu, J. Huang, N. Nasholm, A. He, T. C. Kuo, E. R. B. Sangalang, J. Pons, A. Barkal, R. E. Brewer, K. D. Marjon, J. G. Vilches-Moure, P. L. Marshall, R. Fernandes, M. Monje, J. R. Cochran, P. H. Sorensen, H. E. Daldrup-Link, I. L. Weissman, J. Sage, R. Majeti, C. R. Bertozzi, W. A. Weiss, C. L. Mackall, R. G. Majzner, Anti-GD2 synergizes with CD47 blockade to mediate tumor eradication. *Nat. Med.* **28**, 333–344 (2022).
60. J. Wang, J. Sun, L. N. Liu, D. B. Flies, X. Nie, M. Toki, J. Zhang, C. Song, M. Zarr, X. Zhou, X. Han, K. A. Archer, T. O'Neill, R. S. Herbst, A. N. Boto, M. F. Sanmamed, S. Langermann, D. L. Rimm, L. Chen, Siglec-15 as an immune suppressor and potential target for normalization cancer immunotherapy. *Nat. Med.* **25**, 656–666 (2019).
61. A. T. Yeo, S. Rawal, B. Delcuze, A. Christofides, A. Atayde, L. Strauss, L. Balaj, V. A. Rogers, E. J. Uhlmann, H. Varma, B. S. Carter, V. A. Boussiotis, A. Charest, Single-cell RNA sequencing reveals evolution of immune landscape during glioblastoma progression. *Nat. Immunol.* **23**, 971–984 (2022).
62. Y. Ikehara, S. K. Ikehara, J. C. Paulson, Negative regulation of T cell receptor signaling by Siglec-7 (p70/AIRM) and Siglec-9. *J. Biol. Chem.* **279**, 43117–43125 (2004).
63. D. Dangaj, M. Bruand, A. J. Grimm, C. Ronet, D. Barras, P. A. Duttagupta, E. Lanitis, J. Duraiswamy, J. L. Tanyi, F. Benencia, J. Conejo-Garcia, H. R. Ramay, K. T. Montone, D. J. Powell, P. A. Gimotty, A. Facciabene, D. G. Jackson, J. S. Weber, S. J. Rodig, S. F. Hodi, L. E. Kandalaft, M. Irving, L. Zhang, P. Foukas, S. Rusakiewicz, M. Delorenzi, G. Coukos, Cooperation between constitutive and inducible chemokines enables T cell engraftment and immune attack in solid tumors. *Cancer Cell* **35**, 885–900.e10 (2019).
64. J. M. Romero, B. Grünwald, G. H. Jang, P. P. Bavi, A. Jhaveri, M. Masoomian, S. E. Fischer, A. Zhang, R. E. Denroche, I. M. Lungu, A. De Luca, J. M. S. Bartlett, J. Xu, N. Li, S. Dhaliwal, S. B. Liang, D. Chadwick, F. Vyas, P. Bronsert, R. Khokha, T. L. McGaha, F. Notta, P. S. Ohashi, S. J. Done, G. M. O'Kane, J. M. Wilson, J. J. Knox, A. Connor, Y. Wang, G. Zogopoulos, S. Gallinger, A four-chemokine signature is associated with a T-cell-inflamed phenotype in primary and metastatic pancreatic cancer. *Clin. Cancer Res.* **26**, 1997–2010 (2020).
65. N. Kirchhammer, M. P. Trefny, M. Natoli, D. Brücher, S. N. Smith, F. Werner, V. Koch, D. Schreiner, E. Bartoszek, M. Buchi, M. Schmid, D. Breu, K. P. Hartmann, P. Zaytseva, D. S. Thommen, H. Läubli, J. P. Böttcher, M. A. Stanczak, A. S. Kashyap, A. Plückthun, A. Zippelius, NK cells with tissue-resident traits shape response to immunotherapy by inducing adaptive antitumor immunity. *Sci. Transl. Med.* **14**, eabm9043 (2022).
66. X. Jiao, M. A. Velasco-Velázquez, M. Wang, Z. Li, H. Rui, A. R. Peck, J. E. Korkola, X. Chen, S. Xu, J. B. DuHadaway, S. Guerrero-Rodriguez, S. Addya, D. Sicoli, Z. Mu, G. Zhang, A. Stucky, X. Zhang, M. Cristofanilli, A. Fatatis, J. W. Gray, J. F. Zhong, G. C. Prendergast, R. G. Pestell, CCR5 governs DNA damage repair and breast cancer stem cell expansion. *Cancer Res.* **78**, 1657–1671 (2018).
67. C. Liu, Z. Yao, J. Wang, W. Zhang, Y. Yang, Y. Zhang, X. Qu, Y. Zhu, J. Zou, S. Peng, Y. Zhao, S. Zhao, B. He, Q. Mi, X. Liu, X. Zhang, Q. Du, Macrophage-derived CCL5 facilitates immune escape of colorectal cancer cells via the p65/STAT3-CSN5-PD-L1 pathway. *Cell Death Differ.* **27**, 1765–1781 (2020).
68. R. M. Zemek, W. L. Chin, V. S. Fear, B. Wylie, T. H. Casey, C. Forbes, C. M. Tilsed, L. Boon, B. B. Guo, A. Bosco, A. R. R. Forrest, M. J. Millward, A. K. Nowak, R. A. Lake, T. Lassmann, W. J. Lesterhuis, Temporally restricted activation of IFNβ signaling underlies response to immune checkpoint therapy in mice. *Nat. Commun.* **13**, 4895 (2022).
69. C. Büll, T. J. Boltje, N. Balneger, S. M. Weischer, M. Wassink, J. J. van Gemst, V. R. Bloemendal, L. Boon, J. van der Vlag, T. Heise, M. H. den Brok, G. J. Adema, Sialic acid blockade suppresses tumor growth by enhancing T-cell-mediated tumor immunity. *Cancer Res.* **78**, 3574–3588 (2018).
70. B. Wang, J. Brand-Miller, The role and potential of sialic acid in human nutrition. *Eur. J. Clin. Nutr.* **57**, 1351–1369 (2003).
71. A. Cugurra, T. Mamuladze, J. Rustenhoven, T. Dykstra, G. Beroshvili, Z. J. Greenberg, W. Baker, Z. Papadopoulos, A. Drieu, S. Blackburn, M. Kanamori, S. Brioschi, J. Herz, L. G. Schuettpelz, M. Colonna, I. Smirnov, J. Kipnis, Skull and vertebral bone marrow are myeloid cell reservoirs for the meninges and CNS parenchyma. *Science* **373**, (2021).
72. A. Amorim, D. De Feo, E. Friebel, F. Ingelfinger, C. D. Anderfuhren, S. Krishnarajah, M. Andreadou, C. A. Welsh, Z. Liu, F. Ginhoux, M. Greter, B. Becher, IFNγ and GM-CSF control complementary differentiation programs in the monocyte-to-phagocyte transition during neuroinflammation. *Nat. Immunol.* **23**, 217–228 (2022).
73. A. Silvin, S. Uderhardt, C. Piot, S. Da Mesquita, K. Yang, L. Geirsdottir, K. Mulder, D. Eyal, Z. Liu, C. Bridlance, M. S. Thion, X. M. Zhang, W. T. Kong, M. Deloger, V. Fontes, A. Weiner, R. Ee, R. Dress, J. W. Hang, A. Balachander, S. Chakarov, B. Malleret, G. Dunsmore, O. Cexus, J. Chen, S. Garel, C. A. Dutertre, I. Amit, J. Kipnis, F. Ginhoux, Dual ontogeny of disease-associated microglia and disease inflammatory macrophages in aging and neurodegeneration. *Immunity* **55**, 1448–1465.e6 (2022).
74. M. A. Stanczak, S. S. Siddiqui, M. P. Trefny, D. S. Thommen, K. F. Boligan, S. von Gunten, A. Tzankov, L. Tietze, D. Lardinois, V. Heinzelmann-Schwarz, M. von Bergwelt-Baildon, W. Zhang, H. J. Lenz, Y. Han, C. I. Amos, M. Syedbasha, A. Egli, F. Stenner, D. E. Speiser, A. Varki, A. Zippelius, H. Laubli, Self-associated molecular patterns mediate cancer immune evasion by engaging Siglecs on T cells. *J. Clin. Invest.* **128**, 4912–4923 (2018).
75. B. Kaminow, D. Yunusov, A. Dobin, STARsolo: Accurate, fast and versatile mapping/quantification of single-cell and single-nucleus RNA-seq data. *bioRxiv*, 2021.05.05.442755 (2021).

76. A. T. L. Lun, S. Riesenfeld, T. Andrews, T. P. Dao, T. Gomes; participants in the 1st Human Cell Atlas Jamboree, J. C. Marioni, EmptyDrops: Distinguishing cells from empty droplets in droplet-based single-cell RNA sequencing data. *Genome Biol* **20**, 63 (2019).
77. C. A. Vallejos, D. Risso, A. Scialdone, S. Dudoit, J. C. Marioni, Normalizing single-cell RNA sequencing data: Challenges and opportunities. *Nat. Methods* **14**, 565–571 (2017).
78. A. T. Lun, D. J. McCarthy, J. C. Marioni, A step-by-step workflow for low-level analysis of single-cell RNA-seq data with Bioconductor. *F1000Res.* **5**, 2122 (2016).
79. D. J. McCarthy, K. R. Campbell, Q. F. Wills, A. T. L. Lun, Scater: Pre-processing, quality control, normalization and visualization of single-cell RNA-seq data in R. *Bioinformatics* **33**, 1179–1186 (2017).
80. R. A. Amezquita, A. T. L. Lun, E. Becht, V. J. Carey, L. N. Carpp, L. Geistlinger, F. Martini, K. Rue-Albrecht, D. Risso, C. Soneson, L. Waldron, H. Pages, M. L. Smith, W. Huber, M. Morgan, R. Gottardo, S. C. Hicks, Orchestrating single-cell analysis with bioconductor. *Nat. Methods* **17**, 137–145 (2019).
81. L. Haghverdi, A. T. L. Lun, M. D. Morgan, J. C. Marioni, Batch effects in single-cell RNA-sequencing data are corrected by matching mutual nearest neighbors. *Nat. Biotechnol.* **36**, 421–427 (2018).
82. F. Murtagh, P. Legendre, Ward's hierarchical agglomerative clustering method: Which algorithms implement ward's criterion? *J. Classif.* **31**, 274–295 (2014).
83. P. Langfelder, B. Zhang, S. Horvath, Defining clusters from a hierarchical cluster tree: The Dynamic Tree Cut package for R. *Bioinformatics* **24**, 719–720 (2008).
84. D. Aran, A. P. Looney, L. Liu, E. Wu, V. Fong, A. Hsu, S. Chak, R. P. Naikawadi, P. J. Wolters, A. R. Abate, A. J. Butte, M. Bhattacharya, Reference-based analysis of lung single-cell sequencing reveals a transitional profibrotic macrophage. *Nat. Immunol.* **20**, 163–172 (2019).
85. T. S. Heng, M. W. Painter; Immunological Genome Project Consortium, The Immunological Genome Project: Networks of gene expression in immune cells. *Nat. Immunol.* **9**, 1091–1094 (2008).
86. M. Andreatta, A. Tjitropranoto, Z. Sherman, M. C. Kelly, T. Ciucci, S. J. Carmona, A $CD4^+$ T cell reference map delineates subtype-specific adaptation during acute and chronic viral infections. *eLife* **11**, e76339 (2022).
87. M. Andreatta, J. Corria-Osorio, S. Muller, R. Cubas, G. Coukos, S. J. Carmona, Interpretation of T cell states from single-cell transcriptomics data using reference atlases. *Nat. Commun.* **12**, 2965 (2021).
88. J. Herrero, M. Muffato, K. Beal, S. Fitzgerald, L. Gordon, M. Pignatelli, A. J. Vilella, S. M. Searle, R. Amode, S. Brent, W. Spooner, E. Kulesha, A. Yates, P. Flicek, Ensembl comparative genomics resources. *Database* **2016**, bav096 (2016).
89. S. Müller, G. Kohanbash, S. J. Liu, B. Alvarado, D. Carrera, A. Bhaduri, P. B. Watchmaker, G. Yagnik, E. Di Lullo, M. Malatesta, N. M. Amankulor, A. R. Kriegstein, D. A. Lim, M. Aghi, H. Okada, A. Diaz, Single-cell profiling of human gliomas reveals macrophage ontogeny as a basis for regional differences in macrophage activation in the tumor microenvironment. *Genome Biol.* **18**, 234 (2017).
90. A. T. L. Lun, J. C. Marioni, Overcoming confounding plate effects in differential expression analyses of single-cell RNA-seq data. *Biostatistics* **18**, 451–464 (2017).
91. M. D. Robinson, D. J. McCarthy, G. K. Smyth, edgeR: A bioconductor package for differential expression analysis of digital gene expression data. *Bioinformatics* **26**, 139–140 (2010).
92. M. D. Robinson, A. Oshlack, A scaling normalization method for differential expression analysis of RNA-seq data. *Genome Biol.* **11**, R25 (2010).
93. D. Wu, G. K. Smyth, Camera: A competitive gene set test accounting for inter-gene correlation. *Nucleic Acids Res.* **40**, e133 (2012).
94. A. Subramanian, P. Tamayo, V. K. Mootha, S. Mukherjee, B. L. Ebert, M. A. Gillette, A. Paulovich, S. L. Pomeroy, T. R. Golub, E. S. Lander, J. P. Mesirov, Gene set enrichment analysis: A knowledge-based approach for interpreting genome-wide expression profiles. *Proc. Natl. Acad. Sci. U.S.A.* **102**, 15545–15550 (2005).
95. A. T. Kong, F. V. Leprevost, D. M. Avtonomov, D. Mellacheruvu, A. I. Nesvizhskii, MSFragger: Ultrafast and comprehensive peptide identification in mass spectrometry-based proteomics. *Nat. Methods* **14**, 513–520 (2017).
96. F. Yu, S. E. Haynes, A. I. Nesvizhskii, IonQuant enables accurate and sensitive label-free quantification with FDR-controlled match-between-runs. *Mol. Cell. Proteomics* **20**, 100077 (2021).
97. M. Choi, C. Y. Chang, T. Clough, D. Broudy, T. Killeen, B. MacLean, O. Vitek, MSstats: An R package for statistical analysis of quantitative mass spectrometry-based proteomic experiments. *Bioinformatics* **30**, 2524–2526 (2014).
98. T. D. Schmittgen, K. J. Livak, Analyzing real-time PCR data by the comparative CT method. *Nat. Protoc.* **3**, 1101–1108 (2008).
99. A. R. Pombo Antunes, I. Scheyltjens, F. Lodi, J. Messiaen, A. Antoranz, J. Duerinck, D. Kancheva, L. Martens, K. De Vlaminck, H. Van Hove, S. S. Kjølner Hansen, F. M. Bosisio, K. Van der Borght, S. De Vleeschouwer, R. Sciot, L. Bouwens, M. Verfaillie, N. Vandamme, R. E. Vandenbroucke, O. De Wever, Y. Saeys, M. Guilliams, C. Gysemans, B. Neyns, F. De Smet, D. Lambrechts, J. A. Van Ginderachter, K. Movahedi, Single-cell profiling of myeloid cells in glioblastoma across species and disease stage reveals macrophage competition and specialization. *Nat. Neurosci.* **24**, 595–610 (2021).
100. V. van Unen, T. Höllt, N. Pezzotti, N. Li, M. J. T. Reinders, E. Eisemann, F. Koning, A. Vilanova, B. P. F. Lelieveldt, Visual analysis of mass cytometry data by hierarchical stochastic neighbour embedding reveals rare cell types. *Nat. Commun.* **8**, 1740 (2017).

Acknowledgments: We are grateful to the patients and their families for consent to donate tissues to our brain tumor biobank. Calculations were performed at sciCORE (http://scicore.unibas.ch/) Center for Scientific Computing at University of Basel. We thank A. Zippelius, J. Niess, M. Donath, and R. Nishinakamura for providing genetic mouse lines; M. Muraro for technical help with the perfusion bioreactors; C. Giachino and E. Parmigiani from Verdon Taylor Lab for providing the $PDGF^+Trp53^-$ mouse glioma cell line; P. Shastri, who gave us the 005 cell line as a gift; M. Stanczak for providing the GNE-KO plasmid; A. Bärenwaldt for discussions and advice; and the genomics, proteomics, flow cytometry, and animal core facilities of University of Basel, Switzerland, for technical and logistical support. **Funding:** This work was supported by a Swiss Cancer Research MD-PhD Grant (MD-PhD-4818-06-2019) to P.S. as well an Alumni Medizin Basel grant to P.S.; Swiss National Science Foundation Professorial Fellowship (PP00P3_176974) to G.H.; the ProPatient Forschungsstiftung, University Hospital of Basel (Annemarie Karrasch Award 2019) to G.H.; Swiss Cancer Research Grant (KFS- 4382-02-2018) to G.H.; the Department of Surgery Grant of University Hospital of Basel to G.H. and P.S.; and by the Brain Tumour Charity Foundation, London, UK (GN- 000562) to G.H. **Author contributions:** G.H., H.L., and P.S. conceived and planned the project. P.S. designed, performed, and analyzed most experiments and wrote the manuscript. J.R. and S.H. provided bioinformatical support and performed computational analysis. A.B., S.L., and B.S. performed the automated microscopy-based screening experiment. N.T. helped with the perfusion bioreactor. J.W., N.R.M., R.W., and D.K. performed in vivo experiments. T.A.M., M.-F.R., and T.S. provided input for research design and interpretation and edited the manuscript. M.M. performed and analyzed in vitro experiments. M.W. and T.W. supervised the automated microscopy-based experiments. G.H. and H.L. supervised and coordinated the study and critically revised the manuscript. All authors reviewed the paper and approved its final version. **Competing interests:** G.H. has equity in and is a cofounder of Incephalo Inc. H.L. received travel grants and consultant fees from BMS and Merck, Sharp, and Dohme (MSD), received research support from BMS and Palleon Pharmaceuticals, and is a scientific advisor of Intervenn and Glycoera. **Data and materials availability:** All data associated with this study are in the paper or the Supplementary Materials. The scRNA-seq dataset is available on GEO under accession number GSE212616.

Submitted 27 October 2022
Resubmitted 20 March 2023
Accepted 13 June 2023
Published 19 July 2023
10.1126/scitranslmed.adf5302